Validating a microphysical prognostic stratospheric aerosol implementation in E3SMv2 using the Mount Pinatubo eruption

Hunter Brown[1], Benjamin Wagman[1], Diana Bull[1], Kara Peterson[1], Benjamin Hillman[1], Xiaohong Liu[2], Ziming Ke[3], Lin Lin[2]

5   [1]Sandia National Laboratories, Albuquerque, NM, USA
[2]Department of Atmospheric Sciences, Texas A&M University, College Station, TX, USA
[3]Lawrence Livermore National Laboratories, 7000 East Avenue, Livermore, CA 94550

Correspondence to: Hunter Brown (hybrown@sandia.gov) and Benjamin Wagman (bmwagma@sandia.gov)

Abstract. This paper describes the addition of a stratospheric prognostic aerosol (SPA) capability – developed with the goal of accurately simulating aerosol formation following explosive volcanic eruptions – in the Department of Energy (DOE) Earth Energy Exascale Model, version 2 (E3SMv2). The implementation includes changes to the 4-mode Modal Aerosol Module microphysics in the stratosphere to allow for larger particle growth and more accurate stratospheric aerosol lifetime following the Mt. Pinatubo eruption. E3SMv2-SPA reasonably reproduces stratospheric aerosol lifetime, burden, and aerosol optical depth when compared to remote sensing observations and the interactive chemistry-climate model, CESM2-WACCM. Global stratospheric aerosol size distributions identify the nucleation and growth of sulfate aerosol from volcanically injected SO_2 from both major and minor volcanic eruptions from 1991 to 1993. Modeled aerosol effective radius is consistently lower than satellite and in-situ measurements (max differences of ~30%). Comparisons with in-situ size distribution samples indicate that this underestimation is due to both E3SMv2-SPA and CESM2-WACCM simulating too small of accumulation and coarse mode aerosol 6-18 months post-eruption, with E3SMv2-SPA simulating ~50% the coarse mode geometric mean diameters of observations 11 months post-eruption. Effective radii from the models and observations are used to calculate offline scattering and absorption efficiencies to explore the implications of smaller simulated aerosol size on the Mt. Pinatubo climate impacts. Scattering efficiencies at wavelengths of peak solar irradiance (~0.5 μm) are 10-80% higher for daily samples in models relative to observations through 1993, suggesting higher diffuse radiation at the surface and a larger cooling effect in the models. Absorption efficiencies at the peak wavelengths of outgoing terrestrial radiation (~10 μm) are 15-40% lower for daily samples in models relative to observations suggesting an underestimation in stratospheric heating in the models. The similar performance of CESM2-WACCM and E3SMv2-SPA makes E3SMv2-SPA a viable alternative to simulating climate impacts from stratospheric sulfate aerosols.

1 Introduction

Explosive volcanic eruptions are a significant source of aerosol forcing given their propensity to inject gas and particulate matter into the stratosphere. These gases form long-lived aerosol that can be spread around the globe (Robock, 2000). The impacts of the stratospheric aerosol loading from these eruptions are wide ranging, as exemplified in observational and modeling findings following the Mt. Pinatubo eruption in 1991: ozone depletion (Hofmann et al., 1994; Solomon et al., 1993; Portmann et al., 1996), surface temperature decreases (Parker et al., 1996; Soden et al., 2002), lower stratosphere temperature increases (Labitzke and McCormick, 1992), reduction in global precipitation (Gillett et al., 2004), lowering of global sea-level (Church et al., 2005), increases in cirrus cloud cover (Liu and Penner, 2002; Wylie et al., 1994), as well as increased diffusivity of incoming radiation (Robock, 2000) with resultant impacts on net primary productivity (Gu et al., 2003; Proctor et al., 2018; Greenwald et al., 2006). The extent of these impacts is dependent upon characteristics of the eruption (e.g., magnitude (Marshall et al., 2019)) and climate state (Zanchettin et al., 2022). The foundation of these physical impacts are the stratospheric aerosol microphysical properties and chemical interactions that occur after an explosive volcanic eruption. Being able to accurately simulate these aerosol microphysical and chemical reactions in Earth system models is important for

65 improving the fidelity of simulations. It also enables climate attribution work that clarifies the role of climatic state versus characteristics of the eruption on downstream impacts. As a first step towards this goal, this paper presents a validation of a prognostic volcanic aerosol implementation within the Department of Energy (DOE) Earth Energy Exascale Model version 2 (E3SMv2) (Golaz et al., 2022; Wang et al., 2020), in comparison with version 2 of the Community Earth System Model (CESM2) (Danabasoglu et al., 2020) and observational data from the Mt. Pinatubo eruption.

70 When simulating large-magnitude explosive volcanic eruptions, most climate models use the Global Space-based Stratospheric Aerosol Climatology (GloSSAC) to prescribe aerosol properties from a compilation of satellite, airborne, and ground based observations (Kovilakam et al., 2020; Thomason et al., 2018). While the GLoSSAC dataset provides an accessible approach for incorporating volcanic forcing and validating model performance, prescribed aerosol products have limitations. Limited dataset availability and/or spatial coverage necessitate data interpolation within the forcing dataset, which

75 may not accurately represent the volcanic forcing in some regions (Kovilakam et al., 2020). Additionally, prescribed aerosols will not respond to the dynamic state in free-running coupled climate simulations as the database has been generated from the observed climatic conditions. This artificially constrains the volcanic forcing across ensembles of simulations, and creates a disconnect between volcanic forcing and the actual atmospheric transport patterns, limiting the usability of these simulations for detection and attribution of an evolving impact to the volcanic source. Another limitation is the lack of aerosol

80 microphysical representation and evolution from a volcanic eruption which ignores aerosol indirect effects on clouds and doesn't allow for model feedbacks on aerosol size and lifetime.

Prognostically modeling the formation and evolution of sulfate aerosol from sulfur dioxide (SO_2) injected into the stratosphere is an alternative, more complete approach for simulating volcanic eruptions, with a variety of methods for representing sulfate aerosol mass, size, and number. The simplest approach is to use a bulk aerosol treatment, which prescribes

85 an aerosol size distribution to a predicted aerosol species mass. This was applied to the earliest multi-year simulations of Pinatubo run with the Hamburg climate model ECHAM4 (Timmreck et al., 1999a, b). Most recently, a bulk representation was used in the GFDL Earth System Model (ESM4.1; Dunne et al. (2020)) to show that changes in SO_2 injection height can have the largest impacts on volcanic mass burden and climate forcing (Gao et al., 2023). The most accurate approach to simulating aerosol properties is the sectional (or bin) approach, but this can be computationally limiting depending on the

90 number of aerosol size bins used. English et al. (2013) coupled the sectional Community Aerosol and Radiation Model for Atmospheres (CARMA; Toon et al. (1988)) with version 3 of the Whole Atmosphere Community Climate Model (WACCM3; Garcia et al. (2007)), showing the value of a sectional model in simulating the large variation in aerosol mode size and width that occurs after Pinatubo and larger magnitude eruptions. The modal aerosol approach – representing aerosol size distributions by multiple, evolving lognormal functions – strikes a balance between bulk simplicity and sectional cost. This is used in a

95 stratospheric, prognostic aerosol treatment with interactive ozone chemistry (Mills et al., 2016), developed in the Community Earth System Model (CESM, version 1) (Hurrell et al., 2013) using the version 4 of WACCM (Marsh et al., 2013). This model design has been used to identify the impacts of volcanic eruptions on stratospheric ozone (Ivy et al., 2017; Solomon et al.,

2016), the importance of interactive chemistry on the representation of sulfate formation and distribution following Pinatubo (Mills et al., 2017), as well as effective strategies for geoengineering (Kravitz et al., 2017).

100   Accurate simulation of the stratospheric sulfate size distributions is important for simulating the climate impacts of volcanic eruptions. This is because both the scattering of incoming shortwave energy (i.e., surface cooling) and absorption of outgoing longwave energy (i.e., stratospheric warming) are related to aerosol size and number through Mie theory. Size and number in turn depend on the aerosol modeling approach (e.g., bulk, modal, sectional). In E3SM, tropospheric aerosol is simulated with the 4-mode Modal Aerosol Module (MAM4; Liu et al. (2012, 2016)). In the case of sulfate, MAM4 represents
105   the oxidation of SO_2 to form sulfate aerosol, the further growth of these aerosol through condensation and coagulation into larger aerosol size modes, and the sedimentation of these aerosol through wet and dry deposition.

Here we present a new prognostic aerosol capability implemented within E3SMv2 to enable simulation of the evolution of volcanic stratospheric aerosols and their properties. Similar to Mills et al. (2016), we modify the microphysical treatment of stratospheric aerosol in MAM4. The original validation of this implementation (Mills et al., 2016, 2017) focused
110   on representation of aerosol lifetime, aerosol chemistry, radiative impacts, and dynamical response to the Pinatubo eruption. Here we pay more attention to the aerosol microphysics and how model representations are related to global and regional climate impacts. We use both observations from the 1991 eruption of Mt. Pinatubo as well as CESM2-WACCM to validate the implementation and demonstrate that we can reasonably simulate the lifetime, burden, and aerosol optical depth (AOD) of stratospheric sulfate without the computationally expensive, whole-atmosphere, comprehensive chemistry in WACCM.
115   Additionally, we highlight the importance of simulated aerosol size and number on shortwave and longwave radiative impacts through comparisons of aerosol effective radius and number distributions to in situ observations. Utilizing these effective radii in single particle Mie scattering calculations, we explore how variations in modeled aerosol microphysics affect the volcanic aerosol impacts on diffuse/direct radiation at the surface as well as longwave absorption and heating rates in the stratosphere.

2. Models and Simlations

120   In this work we modify E3SMv2 to include a stratospheric prognostic aerosol capability. We test stratospheric microphysical and chemical implementations in the context of the Mt. Pinatubo eruption and compare to version 2 of the Community Earth System Model CESM2 with the Whole Atmosphere Community Climate Model version 6 (WACCM6; Gettelman et al., 2019).

2.1 E3SMv2

125   Originally a branch from CESM1, E3SMv1 diverged with a focus on computational efficiency, scalability, vertical and horizontal resolution, aerosol and cloud parameterizations, as well as more physically based biogeochemistry, river, and cryosphere models (Leung et al., 2020). Simulations in this study are run with E3SMv2 in which clouds are parameterized with an improved version of the Cloud Layers Unified by Binormals (CLUBB) scheme (Larson, 2017), cloud microphysics

130   are simulated by a two-moment bulk microphysics parameterization (MG2; Gettelman and Morrison, 2015), and mixed phase ice nucleation depends on aerosol type and concentration as well as temperature (Wang et al., 2014; Hoose et al., 2010). Aerosols are simulated with MAM4 (Liu et al., 2016). The explosive volcanic eruption treatment prescribes stratospheric volcanic light extinction from version 1 of the GloSSAC reanalysis dataset (Thomason et al., 2018). Atmospheric chemistry is represented with version 2 of the interactive stratospheric ozone (O_3) model (O3v2; Tang et al., 2021). This model uses

135   linearized stratospheric chemistry (Linoz v2; Hsu and Prather, 2009), which calculates net O_3 production as a function of temperature, local O_3 concentration, and overhead column O_3.

2.1.1 Prognostic aerosol in E3SMv2-PA

In the E3SMv2-PA version of the model, prescribed volcanic extinction is removed and the sulfate aerosol precursor, SO_2, is emitted in the stratosphere. The emitted SO_2 undergoes chemical reactions to form sulfate aerosol and condenses onto

140   the surfaces of preexisting aerosols following the prognostic calculations of MAM4.

In E3SMv2-PA, default MAM4 size modes are employed. All aerosol species are represented by three size modes, shown here with 10th/90th percentile global, annual average number distribution dry diameter ranges from Liu et al. (2012): Aitken (0.015-0.053 µm), Accumulation (0.058-0.27 µm), and Coarse (0.80-3.65 µm). A fourth mode (i.e., primary carbon mode (0.039-0.13 µm)) represents freshly emitted black carbon and organic carbon from combustion, which then ages into the

145   accumulation mode. Aerosol mass and number are used to define a modal geometric mean diameter (D_g). This calculated D_g, in conjunction with a fixed modal geometric standard deviation (s_g), defines the modal number distribution. The modal distributions then evolve based on nucleation (aerosol formation), evaporation (aerosol size reduction), condensation and coagulation (aerosol size growth), and dry/wet deposition (aerosol removal). In E3SMv2-PA, the growth of accumulation to coarse mode aerosol is not included because the troposphere seldom has high enough aerosol mass concentrations to generate

150   such large aerosols through condensation and coagulation. Thus, accumulation mode D_g is allowed to increase until they reach the upper modal threshold ($D_{g,hi}$) whereby the model increases accumulation mode number to maintain $D_{g,hi}$ until D_g begins decreasing.

2.1.2 Prognostic stratospheric aerosol in E3SMv2-SPA

Because MAM4 was designed to accurately represent tropospheric aerosol at their respective concentrations and

155   emission fluxes, the sulfate formation from the massive stratospheric influx of SO_2 from the eruption of Pinatubo is not accurately represented in E3SMv2-PA. In addition to removing prescribed volcanic extinction – as for E3SMv2-PA - further modifications are made to MAM4 to create a prognostic stratospheric aerosol version of E3SMv2 (E3SMv2-SPA) that has improved stratospheric aerosol representation following the Pinatubo eruption. These improvements borrow heavily from changes made to version 1 of CESM (CESM1) with WACCM (Appendix B in Mills et al., 2016), which are present in the

160   default MAM4 version in CESM2-WACCM6. The major modifications to MAM4 include (1) the transfer of aerosol mass and number from the accumulation to coarse mode to increase aerosol size and represent the rapid aerosol growth following the

Pinatubo eruption and (2) adjustment of the coarse mode and accumulation mode s_g and minimum/maximum geometric mean diameters to increase aerosol lifetime. Additional steps were taken to tune the model following the change in the accumulation and coarse mode size properties in (2) which included tuning of dust and seasalt emissions to account for the increased coarse

165 mode lifetime in the model as well as recalculating modal optical properties in MAM4 to account for the changes in aerosol size limits and distribution widths.

Unlike typical tropospheric conditions, explosive volcanic eruptions into the stratosphere provide ample SO_2 mass to drive sulfate aerosol into the coarse mode. To represent this rapid growth and overall larger aerosol diameters in the stratosphere an irreversible accumulation mode number and mass transfer into the coarse mode is added to E3SMv2-SPA. The

170 model calculates the mass and number of particles in the tail of the distribution above a specified size cut off ($D_{g,cut}$) of 0.44 μm, transferring this overshooting number and volume into the coarse mode. The model prohibits transfer from the accumulation mode if $D_g < 0.166$ μm and allows total transfer of the gridcell mass and number when $D_g > 0.47$ μm. In CESM2-WACCM, this transfer is reversible in the stratosphere, with an aqueous sulfuric acid (H_2SO_4) equilibrium pressure that depends on temperature and relative humidity.

175 To improve stratospheric aerosol lifetime in E3SMv2-SPA, the default coarse mode s_g is reduced from 2.0 to 1.2. The default accumulation mode s_g is also reduced, from 1.8 to 1.6, which has a small effect on aerosol lifetime. Additional changes to the aerosol modes allow for overlap between the coarse and accumulation modes and include increasing the accumulation mode $D_{g,hi}$ from 0.44 μm to 0.48 μm and decreasing the coarse mode $D_{g,low}$ from 1.0 to 0.4 μm. Lastly, coarse mode $D_{g,hi}$ is increased from 4.0 μm to 40 μm. See Supplementary Table S1 for a summary of these changes.

180 Most of the above changes have little effect on the tropospheric aerosols, except for changes to the coarse mode, which leads to longer lived coarse mode aerosol due to a reduction in removal rates. To account for this, emissions of dust and sea salt are tuned such that a simulation with perpetual present-day forcing obtains a global average AOD (0.1617) and global average dust AOD (0.0281) comparable to present day remote sensing observations of ~0.17 (Lee and Chung, 2013) and 0.28-0.3 (Ridley et al., 2016), respectively. The modal aerosol optical parameterizations are also affected by changes to the

185 prescribed mode s_g, and the modal optical properties were recalculated with the above modifications using the Ghan and Zaveri (2007) offline code used to generate the original files for CESM/E3SM.

2.2 CESM2-WACCM6

The major CESM2 atmosphere model improvements from CESM1 are the inclusion of CLUBB, MG2 cloud microphysics, MAM4, and orographic wave drag parameterizations (Danabasoglu et al., 2020). These are the same in E3SMv2

190 (Golaz et al., 2022) with the exception of a stratospheric prognostic aerosol treatment in MAM4 in CESM2-WACCM6 (Mills et al., 2016, 2017) (see Section 2.1.2). WACCM6 includes updated atmospheric chemistry, aerosol microphysics, and gravity wave drag parameterizations from previous versions of WACCM. Atmospheric chemistry is treated comprehensively through the whole atmospheric column, representing key chemical species and reactions across the troposphere, stratosphere, mesosphere, and lower thermosphere (Gettelman et al., 2019). Within the stratosphere and mesosphere, WACCM6 explicitly

195   calculates the net production and transport of 97 different chemical species described by nearly 300 reactions (Mills et al.,
2017). This comprehensive chemical treatment is a key difference between CESM2-WACCM6 and E3SMv2 (including
E3SMv2-PA and E3SMv2-SPA), as E3SMv2 prescribes from observationally derived climatologies of OH and other relevant
chemical species in sulfur and ozone chemistry (Hsu and Prather, 2009).

2.3 Simulations

200   E3SMv2 simulations are run from 1990-1993 (1989 discarded for aerosol spinup). The model uses the horizontal and
vertical resolution described in (Golaz et al., 2022) where the dynamics run on a ~110 km horizontal grid, the physics run on
a coarsened ~165 km horizontal grid, and both dynamics and physics use the same 72 layer vertical grid with a model top at
approximately 0.1 hPa. Simulations have prescribed sea ice and sea surface temperatures (Taylor et al., 2000) and nudged U
and V winds to 6-hourly MERRA2 reanalysis data. CESM2-WACCM6 simulations are run over the same time period on a
205   0.95˚x1.25˚ grid over 88 pressure levels (model top at ~4.5×10^{-6} hPa). In addition to nudging model U and V winds to 6-
hourly MERRA2 reanalysis data, these simulations also nudge model temperature to the reanalysis to constrain temperature-
dependent stratospheric chemical reactions.

The SO_2 emissions for explosive volcanic eruptions are from VolcanEESMv3.11, a modified version of Neely III and
Schmidt (2016). The VolcanEE3SMv3.11 dataset contains estimates of SO_2 from volcanic eruptions on a 1.9x2.5-degree
210   latitude by longitude grid, with 1 km altitude spacing from the surface to 30 km. SO_2 emissions are provided in molecules cm^{-3} s^{-1}, and all eruptions occur over a six-hour period. The modifications to Neely III and Schmidt (2016) are described in Mills
et al. (2016) and include a reduction in SO_2 emissions for eruptions over 15 Tg SO_2 by a factor of 0.55 to compensate for
missing ice and ash removal processes. For Mt. Pinatubo, 18-19 Tg of SO_2 erupted in the atmosphere (Guo et al., 2004b) with
only ~10 Tg remaining in the stratosphere for further microphysical and chemical evolution (Kremser et al., 2016). This 10 Tg
215   emission is comparable to observed SO_2 7-9 days after the eruption (Mills et al., 2016). The emission takes place between 18-
20 km, at a single lat-lon grid cell (i.e., no spreading). For all simulations, the VolcanEESMv3.11 file was merged with the
monthly CMIP6 SO2 emissions for non-explosive volcanic sources and then remapped to 1x1 degree.

Table 1 provides a summary of some of the key model characteristics for the different sensitivity studies used in this
work. These studies include: E3SMv2 with prescribed volcanic forcing and no emission of volcanic SO_2 (E3SMv-presc);
220   E3SMv2 with the default MAM4 treatment (i.e., no stratospheric aerosol modifications) and emission of volcanic SO_2
(E3SMv2-PA); E3SMv2 with the prognostic stratospheric aerosol modifications and emission of volcanic SO_2 (E3SMv2-
SPA); and CESM2-WACCM6 with emission of volcanic SO_2 (from herein referred to as CESM2-WACCM).

Table 1: Model details for the simulations used within this study. All simulations are run for 5 years (1989-1993) with 1989 discarded
225   **for aerosol spinup.**

Model Version	Horizontal, Vertical resolution	Nudging	Chemistry	Stratospheric Volcanic Aerosol
E3SMv2-presc	ne30pg2 72 vertical levels (0.01 – 1000 hPa)	U + V winds to MERRA2 Reanalysis	Linear ozone chemistry	• Prescribed volcanic forcing (aerosol extinction; no physical aerosol equivalent) derived from satellite, airborne, balloon, and ground based observations (GLoSSAC V1; Thomason et al., 2018)
E3SMv2-PA	ne30pg2 72 vertical levels (0.01 – 1000 hPa)	U + V winds to MERRA2 Reanalysis	Linear ozone chemistry	• Injection of volcanic SO_2 • Default MAM4 (i.e., no stratosphere-specific modifications)
E3SMv2-SPA	ne30pg2 72 vertical levels (0.01 – 1000 hPa)	U + V winds to MERRA2 Reanalysis	Linear ozone chemistry	• Injection of volcanic SO_2 • Prognostic stratospheric aerosol in MAM4 • Stratosphere-specific accumulation to coarse mode transfer
CESM2-WACCM	0.95˚x1.25˚ 88 vertical levels (4.5×10^{-6} – 1000 hPa)	U + V winds and temperature to MERRA2 reanalysis	Interactive ozone chemistry	• Injection of volcanic SO_2 • Prognostic stratospheric aerosol in MAM4 • Stratosphere-specific, reversible accumulation-to-coarse mode transfer

2.4 Effective radius and Mie scattering calculations

Aerosol size distributions in the model provide information about how MAM4 represents volcanic aerosol evolution and can
230 also help explain changes in radiation balance in the earth system. Here we calculate effective radius and use this in single-
particle Mie scattering to understand how changes in size affect diffuse/direct radiation at the surface and absorption of
longwave radiation in the stratosphere. See Appendices A and B for more details.

3. Observational data sets

In addition to comparing to CESM-WACCM, we also employ observational datasets of sulfate burden, aerosol optical
235   depth (AOD), and microphysical properties (effective radius and size distributions) to substantiate the performance of the
prognostic aerosol capability implemented within E3SMv2. Details of the observational datasets are presented below.

3.1 Sulfate burden

3.1.1 HIRS

The High Altitude Infrared Radiation Sounder (HIRS; Baran and Foot, 1994) is an infrared radiometer measuring
240   surface reflectance at 19 different infrared channels (3.7 – 15 µm) and one solar channel (0.69 µm) from a variety of polar
orbiting NOAA platforms since 1978 (Borbas and Menzel, 2021). This study uses HIRS-derived aerosol mass loading over
the period of May 1991 through October 1993 from Baran and Foot (1994), who used the difference between 8.3 µm (aerosol
sensitive) and 12.5 µm (aerosol insensitive) channels to isolate the transmission through the volcanic plume. To back out
aerosol mass loading, they assumed an average stratospheric sulfate aerosol composition of 75% H_2SO_4 + 25% H_2O, particle
245   size and concentration from dustsonde measurements in July 1991 (Deshler et al., 1992), and a single scattering albedo
calculated from Mie theory by integrating over scattering and extinction coefficients from an assumed lognormal distribution
of radius 0.35 µm and standard deviation 1.6. This data covers 80˚N – 80˚S at 5˚ resolution with a systematic error of ~10%
(±1.4 Tg aerosol) due to assumptions in processing and uncertainty in background concentration. Additional minimum and
maximum aerosol composition bounds are included in this range, namely 59%–77% H_2SO_4.

250   ### 3.1.1 SAGE-3λ

This work also uses stratospheric sulfate burden taken from the SAGE-3l dataset compiled for Phase 6 of the Coupled
Model Intercomparison Project (CMIP6; ftp://iacftp.ethz.ch/pub_read/luo/CMIP6/, last access: 12 January 2023) as reported
in Quaglia et al. (2023). The SAGE-3l dataset uses the Stratospheric Aerosol and Gas Experiment II (SAGE-II; Section 3.3.2)
wavelengths of 0.454, 0.525, 1.024 µm, fitting the measured extinction at these wavelengths to a lognormal size distribution
255   and estimating sulfate mass burden from the number density, mode radius, and width of the distribution (Revell et al., 2017)

3.2 Aerosol Optical Depth

3.2.1 AVHRR

The Advanced Very High Resolution Radiometer (AVHRR; Zhao et al., 2013; Heidinger et al., 2014) is a radiometer
that measures surface reflectance in six spectral bands (0.63, 0.86, 1.6, 3.75, 11, and 12 µm) and has served as a meteorological
260   imaging sensor on the NOAA polar orbiting platforms since 1978. It has a 1.1 km spatial resolution and, during the Pinatubo
eruption period of interest (1990-1994), had 2-4 global views per day (Heidinger et al., 2014). An offline radiative transfer

model is used to determine lookup tables for AOD retrievals. The radiative transfer model assumes fine and coarse mode aerosol properties based on validation of AVHRR with the surface radiometer measurements from the Aerosol Robotic Network (AERONET; Zhao et al., 2002), and uncertainty in the AVHRR AOD is estimated at 11.3 % based on surface

265 AERONET validation (Zhao, Xuepeng, 2022). This work uses monthly, clear-sky AOD retrieved over oceans and regridded to 1˚ resolution. Retrievals are made from channel 1 (0.63 μm) and related to the radiatively equivalent AOD at 0.6 μm through a radiative transfer and surface/atmosphere model (Rao et al., 1989). Detection limits on AOD from the AVHRR range from a minimum of 0.01 and a maximum of 2 (Russell et al., 1996).

3.3 Effective radius and size distributions

270 ### 3.3.1 UARS/SAGE-II (Stenchikov et al., 1998)

This work uses column average effective radius derived from two Upper Atmosphere Research Satellite (UARS; Grainger et al., 1995; Lambert et al., 1997) instruments (the Improved Stratospheric Mesospheric Sounder (ISAMS) and Cryogenic Limb Array Etalon Spectrometer (CLAES)), and SAGE-II extinction data (Stenchikov et al., 1998). The UARS instruments ISAMS and CLAES are limb sounders, reporting aerosol extinction –12.11 μm and 12.66 μm wavelengths,

275 respectively, across altitude profiles above 100 hPa (Lambert et al., 1997). Vertical resolution is approximately 2.5 km and horizontal resolution is about 4˚ (Taylor et al., 1994). These extinction values are then used to derive aerosol effective radius assuming volcanic aerosol size distribution parameters from balloon borne measurements (Deshler et al., 1992, 1993) and a sulfate refractive index corresponding to 75% H_2SO_4 aerosol composition (Grainger et al., 1995; Lambert et al., 1997). Another limb sounder, the SAGE-II (McCormick et al., 1995), reports extinction at the 1.02 μm wavelengths which is then used to

280 derive aerosol number density in the atmosphere. The height resolved number density and effective radius are then used to calculate column average effective radius zonal means at 40˚N and 7˚S from 200 hPa – 10 hPa, reported in Fig. 4 of Stenchikov et al. (1998).

3.3.2 SAGE-II

The SAGE-II (Mauldin et al., 1985) instrument flew from October 1984 to August 2005 on the Earth Radiation

285 Budget Satellite (ERBS), measuring light extinction through the atmospheric limb at seven channels from 0.385 to 1.02 μm. The global coverage is 80˚S-80˚N and 1 km vertical resolution. This work uses aerosol effective radius from SAGE-II version 7 (Damadeo et al., 2013) over the tropics (20˚S-20˚N), limited to 21-27 km (50-20 hPa) due to sparse data at lower altitudes (Quaglia et al., 2023). The effective radius is derived from a combination of extinction inversion algorithms that make use of the extinction ratios between 0.525 and 1.02 μm and assume that the aerosols are spheres with a sulfate composition of 75%

290 H_2SO_4 + 25% H_2O by mass (Damadeo et al., 2013).

3.3.3 WOPC

The balloon-borne University of Wyoming optical particle counter (WOPC; Deshler et al., 1993; Deshler, 1994, 2003) uses particle scattering of white light to measure particle counts across 8-12 channels that range in size from 0.15 – 2 µm (Kalnajs and Deshler, 2022). These particle counts are then fit to unimodal or bimodal size distributions such that they minimize the

295   root mean square error in number concentration between the measured cumulative count and the integral of the size distribution (Deshler, 2003). This instrument was launched from 1989-2013 from a variety of locations across the globe, with the most continuous sampling in Laramie, Wyoming. Instrument uncertainties include: ±10% in concentration and ±10% in aerosol radius, and ±40% in the distribution moments (e.g., surface area, volume, and extinction) (Deshler, 2003; Deshler et al., 2019). In this work we reproduce WOPC aerosol size distributions and derived effective radius over Laramie, WY.

300   ## 4. Results

This section traces model performance from the global to the microphysical, tying the latter to the former through single particle optical properties. The global performance of E3SMv2-SPA stratospheric mass burden (Section 4.1) and AOD (Section 4.2) is determined through comparisons with remote sensing data. Regional comparisons to remote and in situ observations of stratospheric R_{eff} (Section 4.3) identify a model small bias, which is explored in more detail through analysis

305   of aerosol size distributions (Section 4.4). Lastly, model data is compared to individual balloon-borne measurements of aerosol size distributions and R_{eff}, relating the effective single particle scattering (Section 4.5) and absorption (Section 4.6) efficiencies to changes in direct/diffuse radiation at the surface (Section 4.5.1) and longwave heating in the stratosphere (Section 4.6.1).

4.1 Sulfur burden

Figure 1 shows the stratospheric mass burden of the sulfur component of sulfate aerosol in the different model

310   sensitivity tests, the HIRS observational dataset (Baran and Foot, 1994), and the SAGE-3l dataset (Revell et al., 2017). The model data is processed to match the HIRS and SAGE-3l data coverage of 80°N – 80°S above the model lapse rate tropopause height. In MAM4 of E3SM and CESM, sulfate is assumed to be ammonium bisulfate (i.e., $(NH_4)HSO_4$) in the atmosphere (Liu et al., 2012, 2016) (Liu et al., 2012), so the sulfur component is determined by scaling modeled sulfate mass by the ratio of sulfur and ammonium bisulfate mass weights such that $Tg\ S = Tg\ SO_4 * \frac{32.066\ g\ mole^{-1}}{115.11\ g\ mole^{-1}}$.

315   When compared to HIRS and SAGE-3l, E3SMv2-SPA improves the modeled stratospheric aerosol burden over E3SMv2-PA, especially in the years following the Pinatubo eruption. The increased aerosol lifetime in the stratosphere is mainly due to our modifications to the coarse mode s in E3SMv2-SPA. The underestimated aerosol lifetime in E3SMv2-PA is mainly caused by too wide an aerosol number distribution, causing fast sedimentation of the larger coarse mode particles in the upper tail of the distribution. The E3SMv2-SPA tends to overestimate aerosol burden compared to HIRS in the 6 months

320   after Pinatubo but agrees well with the slow decay reported in HIRS and SAGE-3l during 1992. From 1992 onward, stratospheric mass burden in E3SMv2-SPA agrees the best with SAGE-3l, which reports higher burdens in 1993 than HIRS.

E3SMv2-SPA and WACCM are similar in atmosphere and aerosol treatments, but have very different atmospheric chemistry, which seems to impact lifetime.

325   In CESM2-WACCM, the interactive hydroxyl radical (OH) treatment causes OH depletion in the plume as the oxidation of SO_2 to form sulfate aerosol depletes available OH and therefore limits the reaction rate (Mills et al., 2017). This is in contrast to E3SMv2 which assumes an OH climatology unaffected by the oxidation of SO_2. The result is faster depletion of SO_2 and higher initial sulfate concentrations in the stratosphere in E3SMv2 (Fig. S3). The difference in OH treatment can be seen in Fig. 1, marked by the faster increase in stratospheric sulfate burden in E3SMv2-PA and E3SMv2-SPA. Another significant difference between the two chemical treatments is the presence of carbonyl sulfide (OCS) in CESM2-WACCM,

330 which is a largely inert tropospheric chemical species that is oxidized and photolyzed when it enters the stratosphere, forming sulfate. This is a major contributor to non-volcanic stratospheric sulfate and will lead to a higher pre-Pinatubo sulfate concentrations in the stratosphere in CESM2-WACCM than in E3SMv2 (Mills et al., 2016). In Fig. 1, the effect of OCS is shown in larger pre-Pinatubo stratospheric burdens in CESM2-WACCM.

   Figure 1 shows that E3SMv2-SPA performs reasonably well when forming sulfate from SO_2 and simulating increased

335 aerosol lifetimes. The following sections will address how well the model parameterizes the aerosol microphysical properties and their impacts on the global radiative balance.
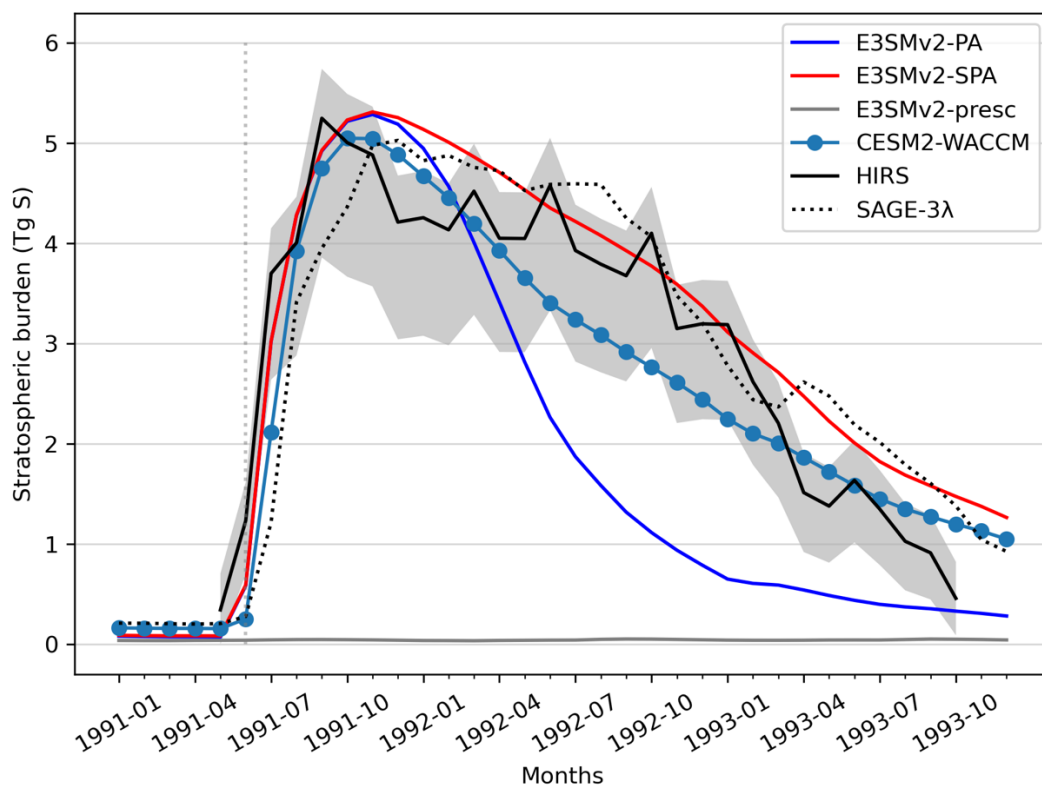
Figure 1: Stratospheric sulfate burden – reported in Tg of the sulfur mass contribution – for model sensitivity tests, as well as HIRS and SAGE-3λ remote sensing observations.

4.2 Aerosol optical depth

In Figure 2, the stratospheric contribution is isolated by subtracting the monthly mean AOD from pre-Pinatubo years, relying on the assumption that non-volcanic background aerosol in the atmosphere is similar in the near-term. Model data is normalized to 1990 monthly means, while AVHRR is normalized to the monthly means for the period June 1989 to May 1991, with the exception of missing data from October-December 1990. Normalized model data is masked to reflect the same temporal and spatial sampling as AVHRR data from 1991-1993 over the oceans only and between 60˚N – 60˚S. Here, AOD from the models is reported at 0.55 µm, while the AVHRR AOD is 0.6 µm.

The AVHRR AOD peaks two months after Pinatubo, linearly decreasing except for periods of flattening in the months March – July 1992 and January – July 1993. The flattening in 1992 is attributed to the continual growth of aerosols due to coagulation, which increases sulfate aerosol scattering efficiency (Russell et al., 1996; Stenchikov et al., 1998) even as aerosol burden continues to decay (Fig. 1). This is supported by a simulated increasing accumulation mode – and to a lesser extent, coarse mode – D_g (Section 4.4; Fig. 4) and a slight increase in global average stratospheric aerosol effective radius (Section 4.3; Fig. 3). The flattening in 1993 for both observations and models may be due in part to the influence of the smaller Chilean volcanic eruption Lascar (1993-01-30; 23.36˚S), which has a discernable impact on modeled global accumulation mode aerosol mean diameters >0.2 µm (Section 4.4; Fig. 4).

In the first year following Pinatubo, AVHRR and the volcanically parameterized models (i.e., E3SMv2-SPA, E3SMv2-presc, and CESM2-WACCM) follow a similar trend, decreasing and leveling off near the beginning of 1992. As for aerosol mass burden, the overly short stratospheric aerosol lifetime in E3SMv2 leads to a rapid decay in AOD. All models consistently underpredict AOD in the first year after the eruption but tend to overpredict AOD in the third year following the eruption. Underprediction may be due in part to a lack of volcanic ash and incorrect number/size representation in the models. Overprediction is likely a factor of aerosol removal assumptions. Of the models, CESM2-WACCM has the closest agreement with AVHRR in 1993, due to a faster decline in AOD than E3SMv2-SPA. This indicates that the comprehensive chemistry in CESM2-WACCM may better represent aerosol size distributions than E3SMv2-SPA (see Section 4.4).

A surprising finding is the close agreement between E3SMv2-SPA and E3SMv2-presc. These models utilize very different approaches: prognostic aerosol microphysics from emitted SO_2 in MAM4 (E3SMv2-SPA) and prescribed stratospheric aerosol extinction from a range of observations in GloSSAC (E3SMv2-presc). This indicates that the changes to aerosol microphysics in MAM4 reasonably recreate the reanalysis data product, especially from 1992 onward.
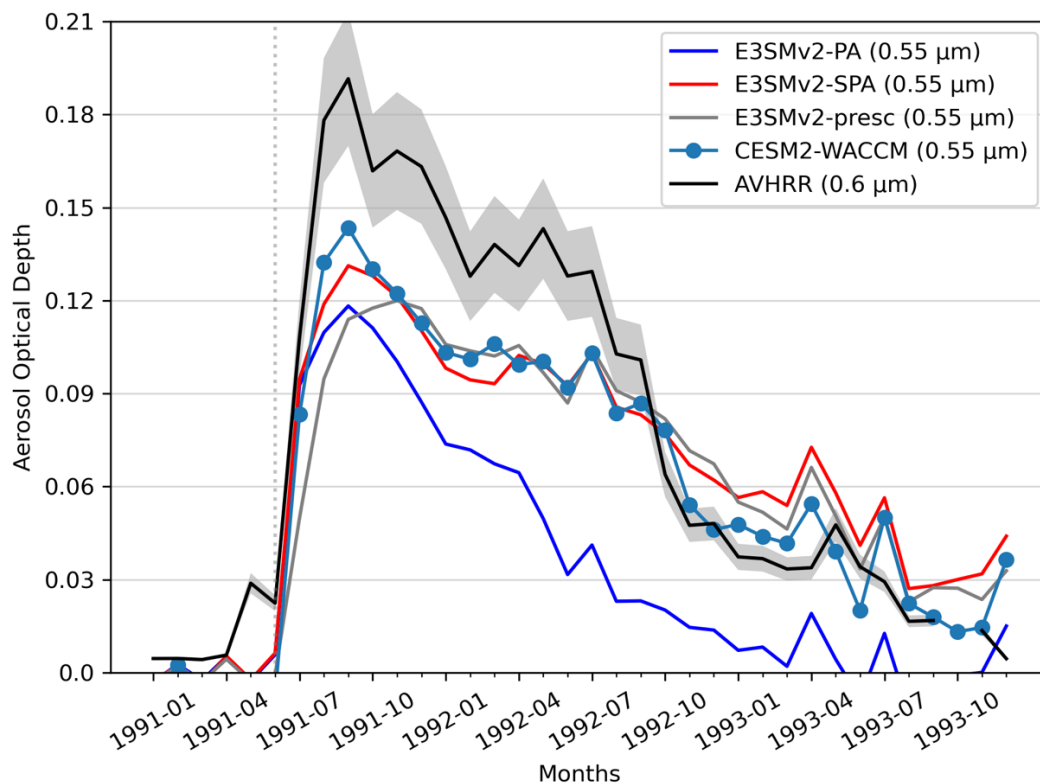
Figure 2: Stratospheric aerosol optical depth (AOD) over the ocean and across latitudes 60˚S–60˚N from the model simulations and
370 **AVHRR. Models calculate AOD at 0.55 μm and AVHRR channel-1 AOD (0.63 μm) is processed to 0.6 μm. Both datasets are**
normalized to volcanically quiescent periods as described in the text. The Pinatubo eruption is marked with the gray dotted line at
1991-06.

4.3 Aerosol effective radius

Effective radius has frequently been used to characterize stratospheric aerosol properties, with stratospheric R_{eff} of
375 less than ~2 μm leading to a net solar radiation scattering effect and surface cooling (Lacis et al., 1992). Based on a range of
in-situ and remote sensing datasets, background stratospheric R_{eff} is estimated at 0.17-0.19 μm, and following Pinatubo reaches
average values of around 0.5 μm with observed values as large as 0.8 or 1.0 μm (Russell et al., 1996, and references therein).
In the month following Pinatubo, there is little change in R_{eff}. This is due to a rapid increase in very small (i.e., Aitken mode
sulfate) and very large (i.e., ash) aerosol particles following the eruption. Enhanced coagulation and condensation, coupled
380 with low sedimentation rates, lead to a steady increase in R_{eff} over the next 3-6 months. Aerosol growth continues until
approximately mid 1992 when R_{eff} peaks, lagging peak values in other metrics such as mass burden and AOD.

Figure 3 shows global R_{eff} (Fig. 3a), in addition to R_{eff} from three different regional zones specific to different
observational datasets: comparisons at 40˚N and 7˚S latitude bands and less than 100hPa with UARS (Fig. 3b), 41˚N 105˚W
between 130-10hPa with WOPC (Fig. 3c), and 20˚S-20˚N between 50-20hPa with SAGE-II (Fig. 3d). Observations tend to
385 measure a minimum size that falls in the middle of the Aitken mode in the model. To account for this characteristic of the data,

the model R_{eff} is an average of effective radii calculated with and without the Aitken mode, with a shaded range between the two R_{eff} represented by shading about the line. Maximum differences tend to occur before Pinatubo, shortly after Pinatubo, and with other volcanic eruptions (e.g., Cerro Hudson (1991-08-08; 45.9˚S)). In Fig. 3a the models reproduce the expected background R_{eff} of 0.17-0.19 μm, and the improvements to aerosol lifetime in E3SMv2-SPA and CESM2-WACCM can be

390 seen in the slower decrease in R_{eff} compared to E3SMv2-PA. There is also a nearly Identical pattern in E3SMv2-SPA and CESM2-WACCM data, but with slightly higher R_{eff} in CESM2-WACCM.

All of the models underestimate R_{eff} compared to observations (Fig. 3b-d). In Fig. 3b, the finer temporal responses to the Pinatubo eruption in the UARS data are less apparent in the model, namely the large peak in R_{eff} at 7˚S associated with short-lived volcanic ash in the stratosphere and the delayed peak at 40˚N and 7˚S due to particle aggregation (Stenchikov et

395 al., 1998). The models neglect volcanic ash contributions, explaining the more gradual particle growth at 7˚S. While the models don't show the same sensitivity to increases in R_{eff} at these latitude bands – possibly due to higher vertical and horizontal spatial scale in the number concentrations from SAGE-II observations – E3SMv2-SPA does show a flattening of the 7˚S R_{eff} akin to the UARS estimate. This corresponds to the eruption of Cerro Hudson in Chile, and the resulting high influx of smaller, Aitken mode particles into the southern stratosphere which drives down R_{eff}. The sensitivity to this eruption in E3SMv2-SPA

400 may be due to higher Aitken mode production in this model than in CESM2-WACCM (see Section 4.4).

The tropical regions tend to have a larger R_{eff} than the midlatitudes in the simulations. This is true of UARS regions 6-12 months after the eruption and also and SAGE-II (tropics; Fig. 3d) data. Theselarger R_{eff} persisting in the tropics a year or more after the eruption. While all models exhibit similar modal aerosol diameters (Fig. S1), the higher R_{eff} is correlated with higher number concentrations in all aerosol modes and a slower decrease in aerosol number (i.e., reduced sedimentation) (Fig.

405 S2). The reduced removal is likely due to higher initial concentrations of SO_2 in the volcanic plume over the tropics (Fig. S3) contributing to more rapid local aerosol growth and a net positive aerosol production. Furthermore, the presence of the upwelling branch of the Brewer-Dobson circulation in this latitude band may help suspend larger aerosol species, slowing aerosol sedimentation rates and increasing their lifetime. The eruption of the Lascar volcano in northern Chile around 1993-02 also contributes to a bump in SO_2, as well as Aitken and accumulation mode aerosol number at the 7˚S band (Fig. S2, S3).

410 When comparing the models to WOPC (Fig. 3c) and SAGE-II (Fig. 3d), E3SMv2-PA has the closest agreement to these datasets in its initial aerosol growth. This growth is more rapid than the other models and leads to a peak in R_{eff} that, while being closer to observed values, drops off precipitously. The R_{eff} in E3SMv2-SPA and CESM2-WACCM have the best agreement with observational values and decay rate a year or more after Pinatubo. Differences across the models are due to the different microphysical assumptions, which can be explored by looking at aerosol size distributions.
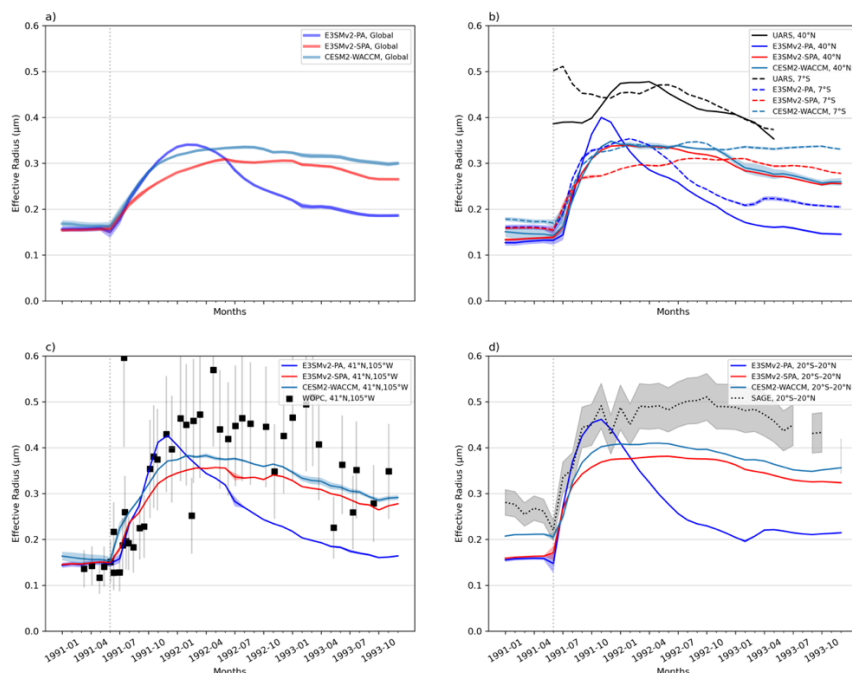
415

Figure 3: Stratospheric aerosol effective radius averaged (a) globally above model tropopause, (b) at 40°N and 7°S and <100 hPa to compare with UARS data (Stenchikov et al., 1998), (c) over Laramie, Wyoming (41°N, 105°W) and 130-10 hPa to match WOPC data (Quaglia et al., 2023), and (d) over 20°S-20°N and 50-20 hPa to match SAGE-II observations (Quaglia et al., 2023). The shaded range in models represents effective radius with and without the Aitken mode, and the model line is an average of the two. Error bars in WOPC data assume a 40% uncertainty and correlation coefficients of 0.5 between aerosol moments and levels (see Appendix A2 in Quaglia et al. (2023)). The Pinatubo eruption is marked with the gray dotted line at 1991-06.

4.4 Aerosol size distributions

While R_{eff} is a good representation of aerosol size in the context of optical properties, it is not always a good indicator for behavior of aerosol microphysical processes. For example, an increase in accumulation mode particle number and a decrease in coarse mode particle number could manifest as an unchanging R_{eff}. An examination of the aerosol size distribution can be more informative when understanding how aerosol chemistry and the MAM4 microphysics contribute to model performance.

Figure 4 shows the globally averaged, stratospheric, aerosol distributions from the three models used in this study and their evolution from 1991 to the end of 1993. The contour fill represents aerosol number (dN/dlogD; cm^{-3}) with dashed and dotted lines indicating modal D_g (μm). In all three models, there is growth in Aitken mode due to new sulfate particle formation following major and minor volcanic eruptions during this period: Pinatubo (1991-06; vertical dotted line), Cerro Hudson (1991-08), Spurr in the Aleutian Islands (1992-06-27; 61.3°N), and Lascar (1993-02). In E3SM (Fig. 4a-b), the prescribed concentrations of OH lead to a rapid oxidation of available SO₂ and higher concentrations of Aitken mode aerosol

compared to CESM2-WACCM (Fig. 4c), resulting in higher aerosol number concentrations in E3SM. It also appears that

435   CESM2-WACCM has higher tropospheric aerosol transport into the stratosphere based on a higher concentration of Aitken mode aerosol across the period of interest. CESM-WACCM has seasonal peak concentrations occurring asynchronous with volcanic eruptions and corresponding to northern hemisphere winter (e.g., 1991 and 1992). The increased Aitken mode number concentration is also seen at 40˚N (Fig. S2). These peaks are attributed to a lower tropopause in Northern Hemisphere winter and may also be due to the inclusion of OCS in CESM-WACCM.

440   The larger volcanic eruptions, Pinatubo and Hudson, inject enough SO_2 into the stratosphere that Aitken mode aerosols grow through condensation and coagulation into the accumulation mode, which then grow through coagulation into the coarse mode. The exception to this is in E3SMv2-PA which lacks the ability to transfer sulfate mass into the coarse mode and so retains a roughly constant coarse mode D_g derived from trace mass (10^{-22}-10^{-21} kg cm^{-3}; global average) and number (10^{-5}-10^{-4} cm^{-3}; global average) concentrations of dust, seasalt, and sulfate aerosol advected from the troposphere (Note: mass

445   and number are related to aerosol size through Equations S1 and S2 in the Supp. Material). Aerosol growth through the modes can be seen in increased number and an increasing trend in aerosol size. Dips in modal D_g correspond to sudden increases in aerosol number (e.g., Aitken mode nucleation from freshly injected SO_2, transfer of a large aerosol number from Aitken to accumulation mode) while mass remains relatively unchanged. This leads to a division of mass across a larger number of aerosols and a subsequent decrease in D_g.

450   Overall, the aerosol modal diameters are similar across the three models, but slight differences exist. There are slightly larger accumulation mode and coarse mode D_g in CESM2-WACCM (0.262 μm; 0.843 μm) than E3SMv2-SPA (0.259 μm; 0.749 μm). This could be a factor of the interactive chemistry in CESM2-WACCM leading to fewer Aitken mode aerosol that initially grow faster through condensation given the longer lived SO_2 in the stratosphere. Contrast this with E3SM where more numerous, smaller aerosol consume the available SO_2 more quickly. The E3SMv2-PA model accumulation mode D_g reaches

455   a higher maximum D_g (0.285 μm) than E3SMv2-SPA or CESM2-WACCM (~0.26 μm). This is due to the missing coarse mode treatment in this model coupled with a larger $D_{g,hi}$ (Section 2.1.2). The result is an accumulation mode that grows to $D_{g,hi}$ following Pinatubo, whereby number is increased to maintain this size instead of transferring mass and number to a larger mode. This also explains the better initial agreement in R_{eff} between E3SMv2-PA and observations in Fig. 3b-d.

         Figure 5 compares modeled aerosol size distributions to in-situ measurements from WOPC, tracking the evolution of

460   a slice of the plume from pre-Pinatubo (1991-04-19) to the end of 1993 (1993-11-16). Daily samples taken with the WOPC over Laramie, WY at a single level (18 km; roughly corresponding to the peak plume R_{eff} across the period (Fig. S4)) are used to validate daily data from E3SMv2-PA and E3SMv2-SPA. Modal D_g (vertical lines) and dN/dlogD are denoted by dotted and dashed lines, as in Fig. 4. Effective diameter (D_{eff}) for models and WOPC are included to relate the changing distributions to aerosol-light interactions.

465   What follows is a breakdown of Fig. 5 into a rough timeline evolution in aerosol size distributions and D_{eff}:

- Pre-Pinatubo conditions (Fig. 5a) are very similar between E3SMv2-PA and E3SMv2-SPA, and the D_{eff} are nearly identical between model and observations. CESM2-WACCM has higher background number concentrations than E3SM.

- One month after Pinatubo (Fig. 5b), all datasets exhibit rapid growth in the smaller diameter aerosols, with some growth in the modeled accumulation mode but little sign of the coarse mode in E3SMv2-SPA. CESM2-WACCM has a massive increase in Aitken and accumulation mode number, possibly due to transport of SO_2 and Aitken mode aerosol into the region from the tropics. This Aitken mode peak is also seen at 17 and 19 km levels (Fig. S5-S6), and results in a decrease in R_{eff} over this height range (Fig. S4). The D_{eff} are still similar across the different datasets, with the exception of CESM2-WACCM which is smaller due to the Aitken mode influence.

- Six months after the eruption (Fig. 5c), a clear coarse mode signal emerges in WOPC, E3SMv2-SPA, and CESM2-WACCM along with a sharp increase in modeled accumulation mode number. Models and WOPC are all comparable in their bimodal D_g and accumulation mode number, while WOPC coarse mode has lower number than E3SMv2-SPA and CESM2-WACCM. E3SMv2-PA has a larger D_{eff} than other datasets (though it is still within the uncertainty of WOPC D_{eff}). This peak in D_{eff} – which is also noted in R_{eff} in Fig. 3 – is attributed to a wider accumulation mode and larger modal D_g in E3SMv2-PA. CESM2-WACCM has larger modal number than all other datasets.

- 11 months after the eruption (Fig. 5d), the WOPC data continues to grow in accumulation and coarse mode. Accumulation mode number is decreasing while coarse mode is increasing in E3SMv2-SPA, suggesting conversion of accumulation mass into the longer-lived coarse mode. The WOPC coarse mode D_g (1.92±0.19 μm) is more than twice that of E3SMv2-SPA (0.828 μm), while the WOPC accumulation mode best-fit (D_g=0.909±0.09 μm, s_g=1.23) is close to E3SMv2-SPA coarse mode (D_g=0.828 μm, s_g=1.2) and is nearly identical to the CESM2-WACCM coarse mode (D_g= 0.918 μm, s_g=1.2). . The overall larger aerosols in the WOPC distributions lead to largest difference in D_{eff} between model and WOPC.

- For one year and longer after the eruption, accumulation mode in E3SMv2-PA is on a steady and rapid decay that can be tracked in size and number (Fig. 5d-i). Over this period, E3SMv2-SPA and CESM2-WACCM generate very similar size distributions, with slightly lower coarse mode number and slightly larger coarse D_g in CESM2-WACCM. Overall, WOPC and E3SMv2-SPA/CESM2-WACCM have similar distributions and similar D_{eff}, with E3SMv2-SPA showing slightly smaller D_{eff} but still within the uncertainty of WOPC data. A peak in Aitken mode aerosol in the models in Fig. 5h may be due to the Lascar eruption in 1992-02.

The previous timeline shows an improved aerosol evolution in E3SMv2-SPA compared to WOPC and exhibits the similarities between CESM2-WACCM and E3SMv2-SPA. It also indicates that E3SMv2-SPA doesn't simulate large enough aerosol compared to the observations. Similar behavior in D_{eff} and relative size bias is noted at 17 km, 19 km, and 20 km levels as well (Fig. S5-S7). Given that the model is nudged to meteorology and that the aerosol in the stratosphere tend to evolve relatively slowly over time, it is assumed that the resolution artifacts of comparing a 1°x1° model grid cell to in-situ

500 measurements are minimal. The impact of this size bias on aerosol climate impact is now explored through effective single particle scattering.
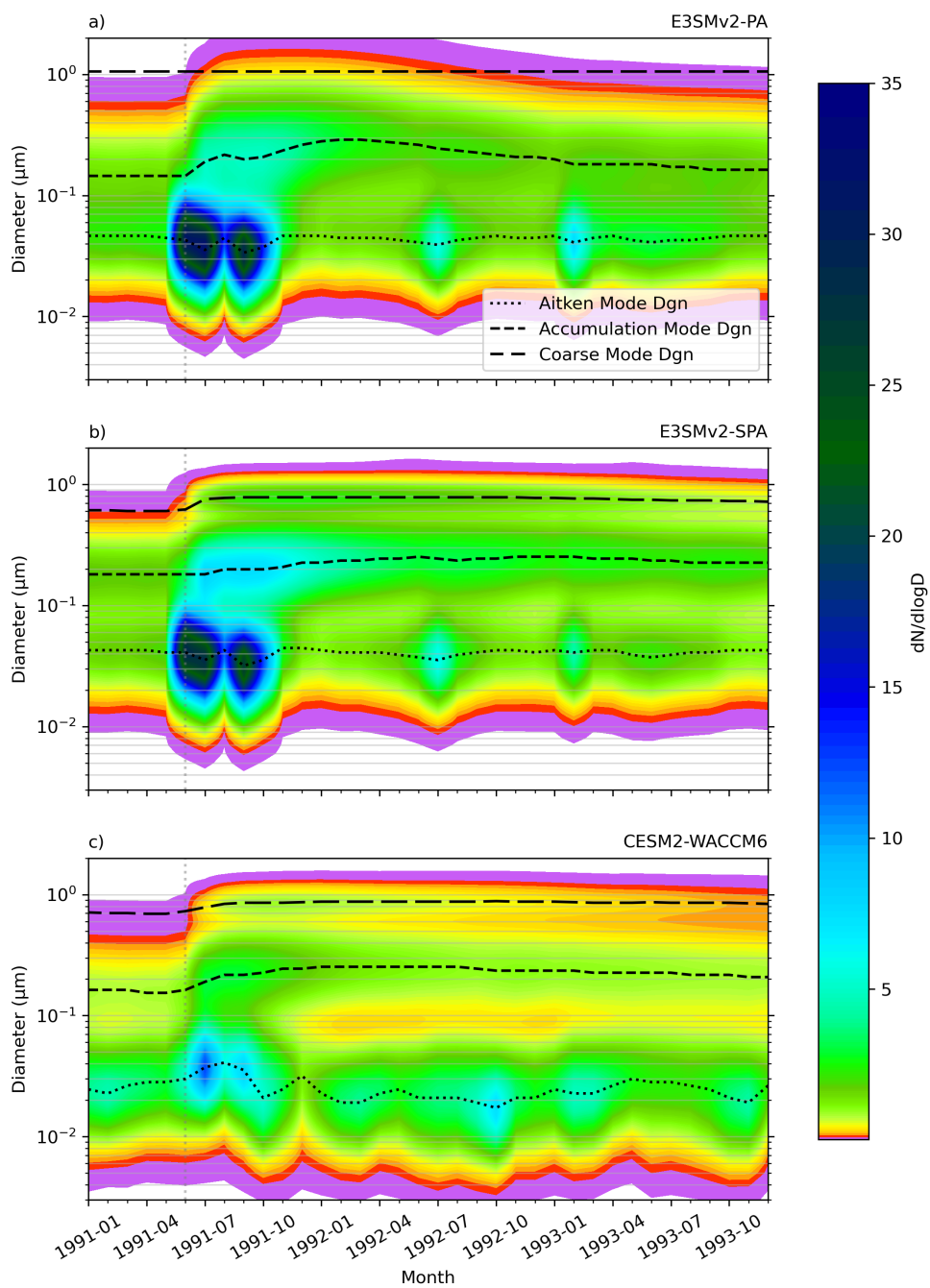
Figure 4: Globally averaged, stratospheric lognormal aerosol size distributions from 1991-1993 for E3SMv2-PA, E3SMv2-SPA, and CESM2-WACCM. The dotted, dashed, and long-dashed lines indicate geometric mean diameters of the Aitken, Accumulation, and Coarse aerosol modes, respectively. The color contour is lognormally scaled. The Pinatubo eruption is marked with the gray dotted line at 1991-06.
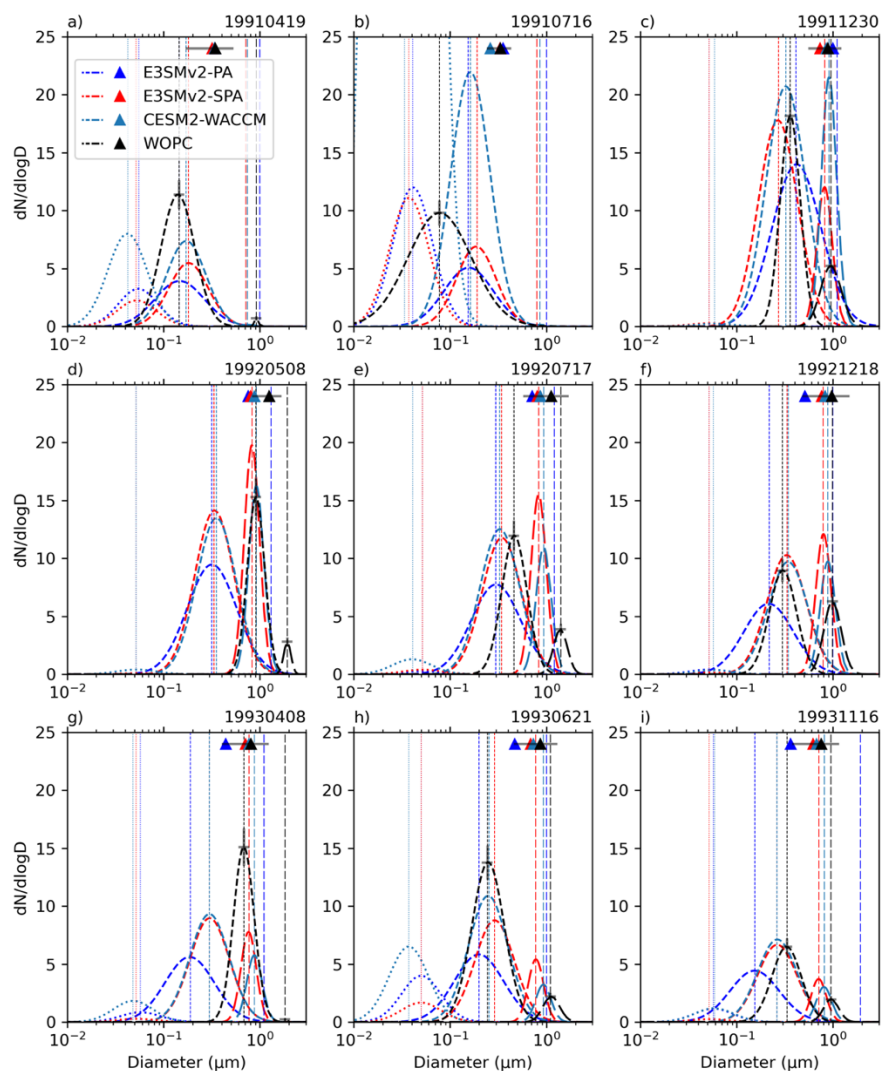
Figure 5: Stratospheric aerosol size distributions from E3SMv2-PA (blue), E3SMv2-SPA (red), and WOPC (black) from 1991-1993. WOPC launches chosen to correspond to spring, summer, and winter measurements for each year, and samples are taken from the 18 km measurements and matched to the nearest model height and grid cell over Laramie, WY (41.3°N, 105°W). The dotted, dashed, and long-dashed lines indicate geometric mean diameters (vertical) and dN/dlogD size modes of the Aitken, Accumulation, and

Coarse aerosol modes, respectively. Triangles denote effective diameters derived from the size distributions. Uncertainties in WOPC diameter, number, and effective diameters are denoted by grey bars at the peak of the distributions and on the markers. Note: anomalously large max number in CESM2-WACCM Aitken mode (376.5 cm^{-1}) is out of the plotting bounds.

515   4.5 Single particle scattering efficiency

The R_{eff} can be used to characterize the evolving aerosol size distribution, which conveniently can be used in the offline calculation of single particle optical properties using Mie theory. Figure 6 shows the scattering efficiency (Q_s) of sulfate particles of size R_{eff} for the same time and height samples as Fig. 5. Additionally, this plot marks the approximate wavelength of peak solar black-body irradiance (λ_{solar}=0.5 µm) to identify when aerosol scattering of solar radiation has the largest impact

520   on radiative balance. Q_s is proportional to the x_{eff}^{4} (i.e., λ^{-4}) (Petty, 2006). This scattering feature can be seen in Fig. 6 where, as wavelengths increase, you will get a rapid decrease in Q_s.

The peak in Q_s shifts from λ of ~0.2 µm before and shortly after Pinatubo (Fig. 6a-b), to 0.5-0.7 µm 6 months after the eruption (Fig. 6c) with the onset of rapid particle growth. For the remainder of the time (Fig. 6d-i), E3SMv2-SPA and CESM2-WACCM R_{eff} result in a Q_s peak right around λ_{solar}, indicating a very efficient scattering of sunlight by these simulated

525   aerosols. The WOPC reports larger R_{eff} than the models, which have a Q_s that is 10-80% higher than observations at λ_{solar} during 1992 (Fig. 6d-f), becoming more similar during 1993 with the decay of stratospheric R_{eff} (Fig. 6g-i). E3SMv2-PA has a similar Q_s to E3SMv2-SPA/CESM2-WACCM until the end of 1992 (Fig. 6f) when there is a quick progressive drop in R_{eff} due to rapid stratospheric aerosol deposition.

These results indicate an optimal sulfate scattering R_{eff} of ~0.3-0.4 µm, which is similar to estimates of the optimal

530   sulfate aerosol size of 0.3 µm in geoengineering applications (Dykema et al., 2016). Given that WOPC predicts larger R_{eff} and smaller Q_s at λ_{solar} 6-18 months after Pinatubo, our results suggest that E3SMv2-SPA/CESM2-WACCM overestimates aerosol scattering and the global cooling effect of the Pinatubo aerosol at this level. Figure 6 relates size distribution differences in models and WOPC to climate impact at a single level. For a better validation of the stratospheric plume and to see if the model disagreement changes when looking across multiple levels, the next step is to calculate Q_s from the stratospheric R_{eff}.

535   Figure 7 shows monthly Q_s generated from averaged stratospheric R_{eff} at a midlatitude site (41˚N 105˚W) (Fig. 3c) and the tropics (Fig. 3d). As in Fig. 6, a similar pattern is shown where smaller modeled R_{eff} lead to higher modeled Q_s at λ_{solar} than observed Q_s. However, the differences between modeled and observed Q_s at λ_{solar} are not as stark for the monthly, stratospheric average values, with max differences on the order of 5-14% as opposed to the 10-80% seen in the daily, 18 km level data. The larger R_{eff} in the tropics leads to a higher Q_s at λ_{solar} one month after Pinatubo (Fig. 7b), and lower Q_s at λ_{solar}

540   18 months after Pinatubo (Fig. 7f), than midlatitude measurements in the stratosphere. The E3SMv2-SPA and CESM-WACCM maximum Q_s from both regions hover around λ_{solar}, with higher modeled Q_s at λ_{solar} in the tropics 2 years after the eruption (Fig. 7h) due to a consistently larger R_{eff} in this region.
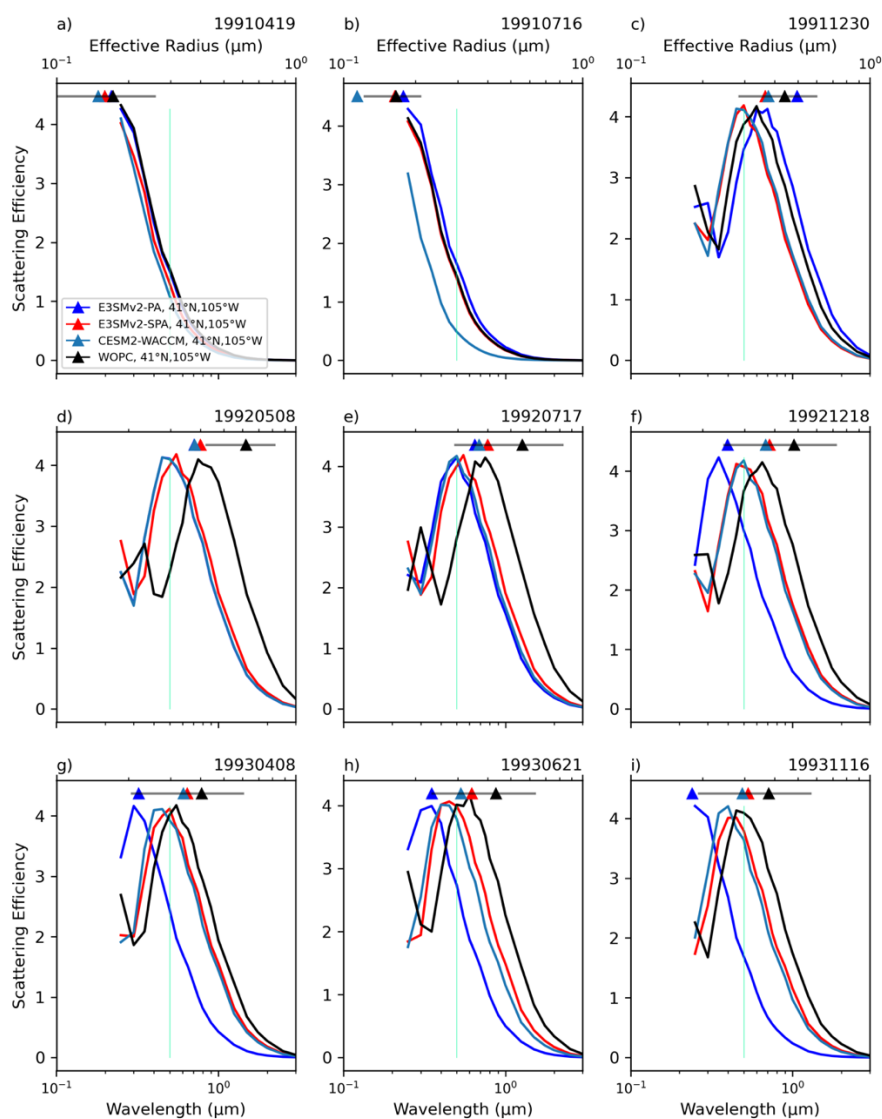
Figure 6: Daily 18 km scattering efficiency (Q_s) using effective size parameter ($x_{eff} = 2\pi R_{eff}/\lambda$) and sulfate refractive index at 0% relative humidity (Hess et al., 1998). Effective radius (R_{eff}) from E3SMv2-PA, E3SMv2-SPA, and WOPC are from Fig. 3c, and are marked by colored triangles at the top of the plot. The bottom x-axis is wavelength (λ; 0.1–3 µm). The top axis is R_{eff} (0.1-1 µm) used in the calculation of Q_s via the effective size parameter (x_{eff}). The turquoise vertical line marks the solar black body wavelength of maximum irradiance (0.5 µm).

545
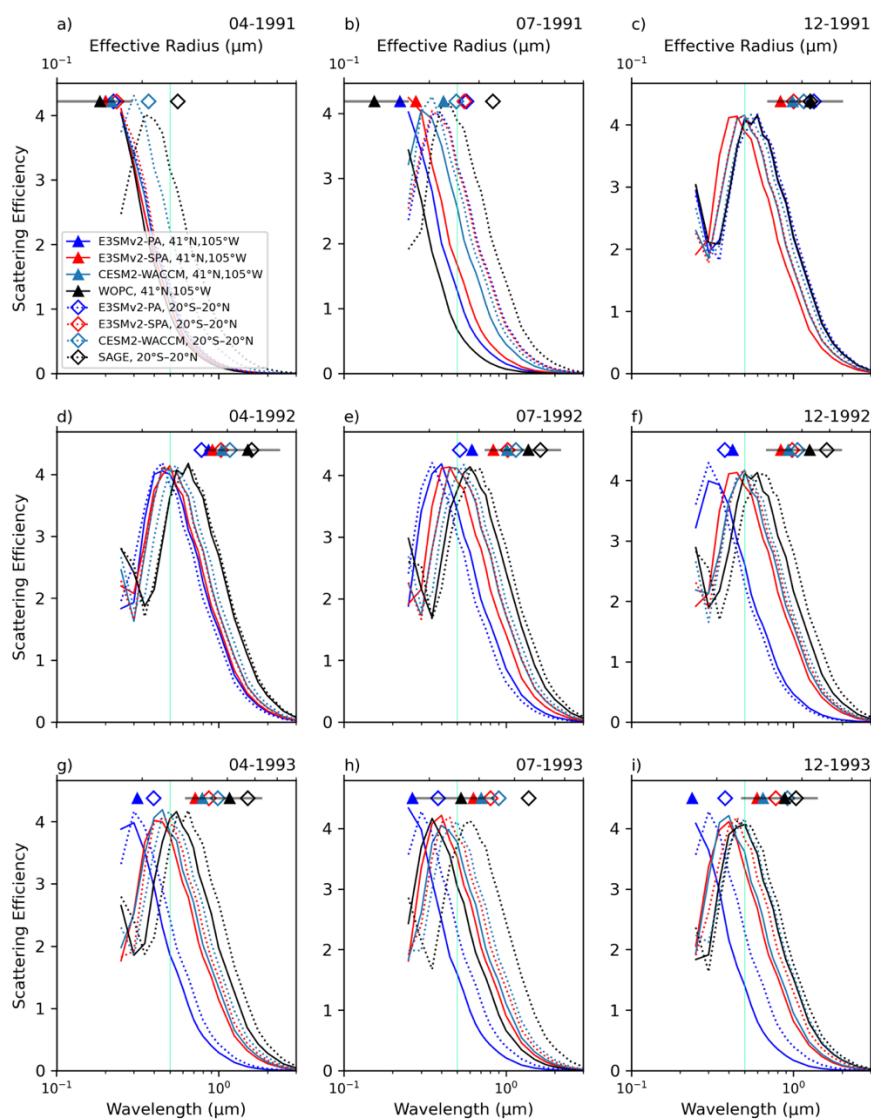
Figure 7: Monthly stratosphere scattering efficiency (Q_s) using effective size parameter ($x_{eff} = 2\pi R_{eff}/\lambda$) and sulfate refractive index at 0% relative humidity (Hess et al., 1998). Monthly R_{eff} are from E3SMv2-PA, E3SMv2-SPA, CESM2-WAACCM, WOPC, and SAGE-II from Fig. 3c-d, and are marked by colored triangles (41˚N 105˚W; WOPC) and hollow diamonds (20˚S–20˚N; SAGE-II) at the top of the plot. The bottom x-axis is wavelength (λ; 0.1–3 µm. The top axis is R_{eff} (0.1-0.7 µm) used in the calculation of Q_s via the effective size parameter (x_{eff}). The turquoise vertical line marks the solar black body wavelength of maximum irradiance (0.5 µm).

4.5.1 Direct / diffuse radiation

The differences in R_{eff} between the different model and observational datasets ultimately affect diffuse and direct radiation at the surface by changing AOD and other aerosol optical properties. In scattering incoming shortwave, a small

560 fraction of light is scattered back to space reducing the amount of energy incident to Earth. The forward scattered SW radiation increases the diffusivity of incident radiation. The Mauna Loa observatory documented a lessening of the direct beam and increase in the diffuse radiation after the eruption of Mt. Pinatubo (Robock, 2000), and globally there was a 21% reduction in direct and a 20% increase in diffuse radiation at the surface (Proctor et al., 2018).

The model simulations use a two-stream approximation for calculating multiple scattering in the atmosphere (Iacono

565 et al., 2008; Neale et al., 2012), which calculates diffuse and direct radiation at the surface from incident radiation, AOD (i.e., the column integrated b_s (Eq. B2)), single scattering albedo (SSA; Fig. S8), and aerosol asymmetry parameter (g; Fig. S9). In a general sense, the input aerosol optical properties determine what fraction of direct radiation makes it through the aerosol layer (AOD), how much of the incident radiation is absorbed in the aerosol layer (1-SSA), and the degree to which the radiation is scattered by the aerosol layer (g).

570 Figure 8 shows the perturbation in diffuse and direct radiation at the surface due to the Pinatubo aerosol layer in the visible to ultraviolet wavelengths (with similar behavior in the near-infrared (Fig. S10)). The values are averaged over the whole earth (Fig. 8a), the 41˚N latitude band (Fig. 8b), and 20˚S-20˚N tropical region (Fig. 8c). There is an increase in diffuse radiation across all of the models and a mirrored decrease in direct radiation. These changes track the increasing R_{eff} (Fig. 3) and the enhanced $Q_s(\lambda)$ (Fig. 7). The magnitude of the direct radiation loss tends to be larger than the increase in diffuse

575 radiation at the surface because some of the scattered incoming solar radiation is lost to space. In all regions, E3SMv2-SPA and CESM2-WACCM have more diffuse and less direct radiation than E3SMv2-PA, the latter of which rapidly approaches zero as the aerosol are removed from the atmosphere. The peak direct and diffuse influence occur in the tropics (Fig. 8c) prior to the 41˚N band (Fig. 8b) as aerosol transport to northern latitudes relies on stratospheric circulation. In the 41˚N band (Fig. 8b) CESM2-WACCM has a higher proportion of diffuse radiation at the surface than all of the other models.

580 Diffuse radiation is not only attributed to aerosol size and material properties – as is Q_s in Fig. 7 – but is also related to the aerosol number concentration. As a result, AOD serves as a good indicator of diffuse/direct radiation at the surface as it accounts for both number and Q_s. Figure 9 shows AOD over the same spatial regions as Fig. 8. The AOD behaves very similarly to diffuse radiation. As in Fig. 8b, Fig. 9b shows CESM2-WACCM with higher AOD over the 41˚N band. This is attributed to both the larger aerosol R_{eff} (Fig. 3c) and higher accumulation and coarse mode number concentrations (Fig. S2a)

585 in CESM2-WACCM. The higher number concentrations are correlated with more SO_2 transport into the midlatitudes in CESM2-WACCM (Fig. S3b), which is likely due to slower oxidation of SO_2 in CESM2-WACCM due to the aforementioned OH depletion in this model.

The impact of clouds on diffuse/direct radiation in the midlatitudes shows up in Fig. 8b, with peaks in normalized total cloud cover (right axis) corresponding to diffuse (direct) radiation peaks (troughs), especially in the late spring/early summer of 1992 and 1993. The approximate co-location of peaks in cloud cover (Fig. 8b) and AOD (Fig. 9b) in the midlatitudes in June of 1992 and 1993 may indicate the presence of aerosol indirect effects. This is consistent with findings by Liu and Penner (2002) which show high rates of homogeneous ice nucleation persisting in the northern midlatitudes through July 1992.

Lastly, E3SMv2-presc has good agreement with E3SMv2-SPA and CESM2-WACCM when compared globally or in the tropics, but reports ~60% the modeled magnitudes for diffuse/direct radiation and ~40-60% modeled AOD in the midlatitudes (Fig. 8 and 9, respectively). This may be due to our use of an older version of the GLoSSAC dataset (Thomason et al., 2018) in which higher latitudes have a low bias in AOD attributed to linear interpolation of the SAGE-II data (Kovilakam et al., 2020).
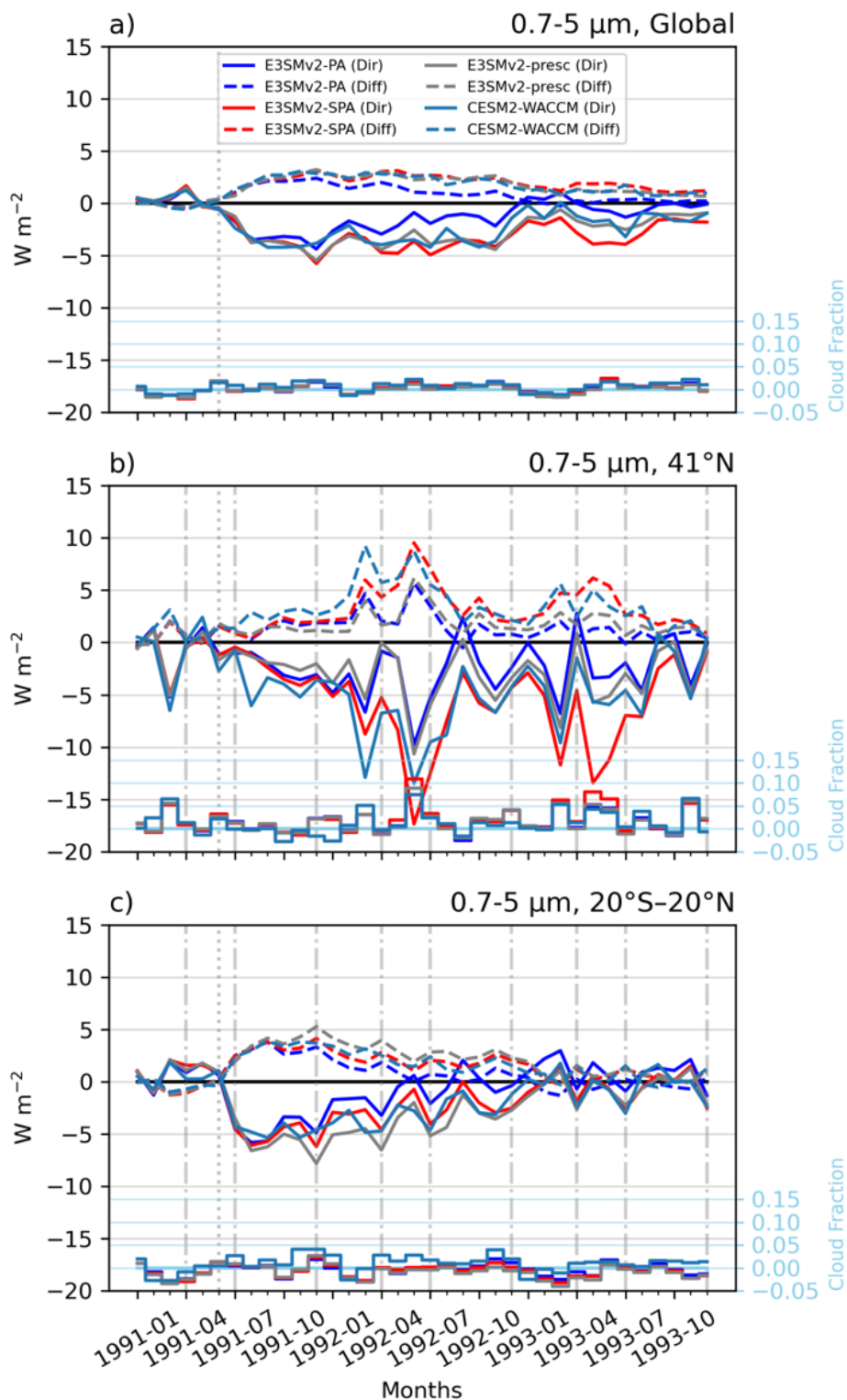
600   **Figure 8: Pinatubo induced changes in diffuse and direct solar radiation at the surface in the 0.2-0.7 μm band (left axis), and total cloud cover fraction (right axis; blue). Regions include global (a), midlatitude band (b; 41˚N), and tropical band (c; 20˚S-20˚N) averages. The Pinatubo eruption is marked with the gray dotted line at 1991-06, and the sample months for Fig. 7 are marked with the gray dash-dot lines. The data is normalized to 1990 monthly means.**
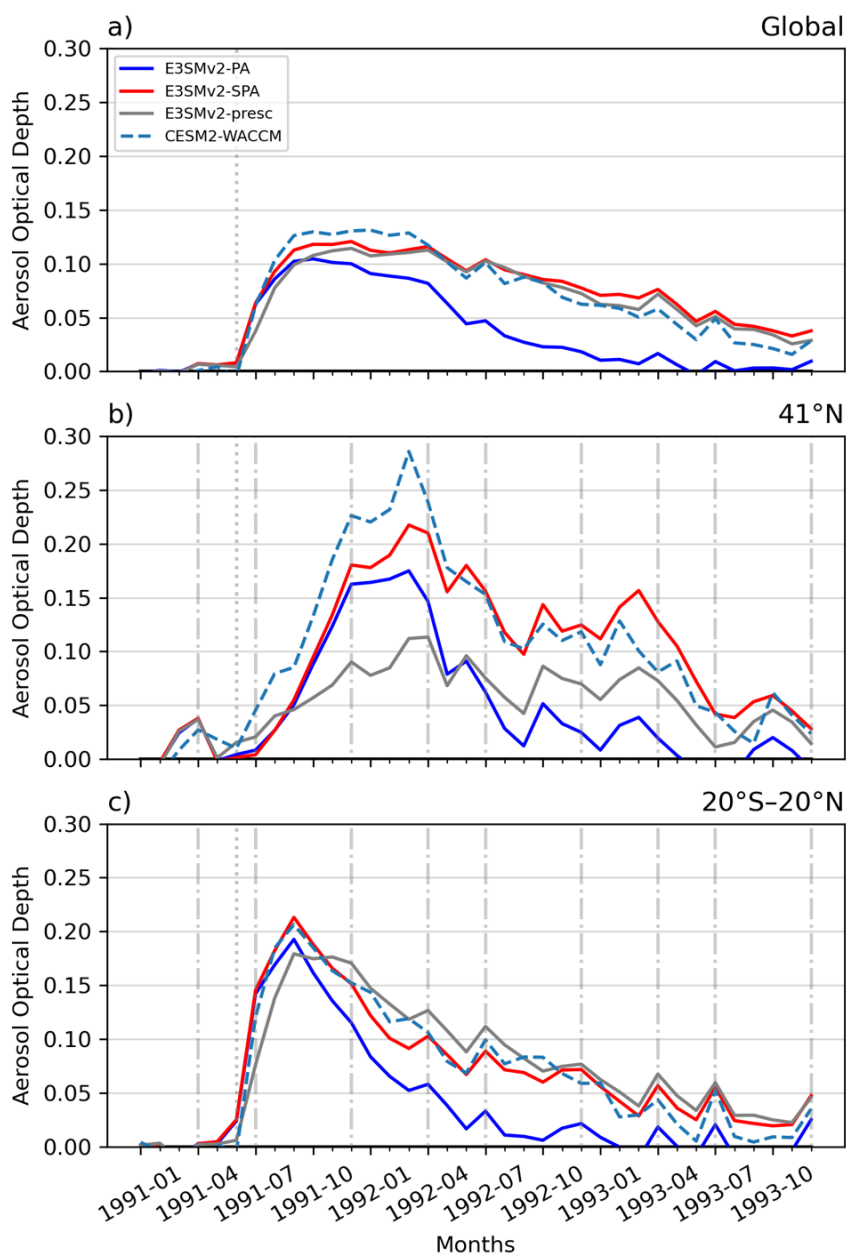
Figure 9: Pinatubo induced changes in aerosol optical depth (AOD) at 0.55 µm. Regions include global (a), midlatitude band (b; 41°N), and tropical band (c; 20°S-20°N) averages. The Pinatubo eruption is marked with the gray dotted line at 1991-06, and the sample months for Fig. 7 are marked with the gray dash-dot lines. The data is normalized to 1990 monthly means.

605

4.6 Single particle absorption efficiency

While the Pinatubo eruption resulted in a net climate cooling effect due to increased scattering, it also contributed to
610 stratospheric warming through the absorption of outgoing longwave radiation within the aerosol layer (Kinne et al., 1992).
Figure 10 shows the Q_a calculated from R_{eff}, with a dark red line indicating the wavelength of peak terrestrial black-body
irradiance (10 μm; λ_{earth}). Sulfate is not an effective absorber at visible wavelengths ($Q_a = 0$ at λ_{solar}) and the determining factor
in stratospheric heating is the magnitude of Q_a at λ_{earth}. The wavelength dependence of Q_a is weaker than Q_s, (proportional to
x_{eff} (i.e, λ^{-1})) and is strongly tied to the imaginary part of n_{Hess}. The proportionality to x_{eff} is denoted in Fig. 10 by the linear
615 increase in $Q_a(\lambda)$ with increasing R_{eff}; the dependence on the imaginary part of n_{Hess} is reflected in the unchanging pattern in
absorption magnitudes for all datasets and times.

In Fig. 10, the linear dependence of Q_a on R_{eff} means that an individual particle in the tropics has more absorption
than the midlatitudes across the whole period, and the observations will have more absorption than the models. This is
explained by the effective radii in these two regions at the top of each panel. For example, the smaller modeled R_{eff} at 41˚N
620 leads to a modeled Q_a that is 15-30% lower than WOPC through 1992 (Fig. 10c-f).

Because the same refractive index is used across all models and observational datasets, the differences in Q_a are due
only to differences in aerosol size. However, this is a simplifying assumption for the modeled Q_a due to their explicit calculation
of the soluble aerosol refractive index (n_s) in the stratosphere based on aerosol water and sulfate content (Eq. B4). E3SM
simulates a stratosphere with unrealistically low stratospheric water vapor (Keeble et al., 2021; Jablonowski et al., in prep)
625 which results in aerosol that are mostly sulfate (Fig. S11) with a refractive index similar to n_{Hess} (Appendix B). Higher water
vapor in CESM2-WACCM means that the assumption of n_{Hess} in calculation of Q_a doesn't account for the volume-weighting
of the hydrated aerosol refractive index (Appendix B). When interstitial stratospheric water and sulfate are used to calculate a
volume-weighted n_s using n_{Hess} and n_{wat}, Q_{abs} at l_{earth} is smaller than that reported with only n_{Hess} by ~12-19% over the 41˚N
band and ~13-17% over 20˚S–20˚N (Table S3). This is due to a smaller magnitude imaginary refractive index for water at this
630 wavelength.
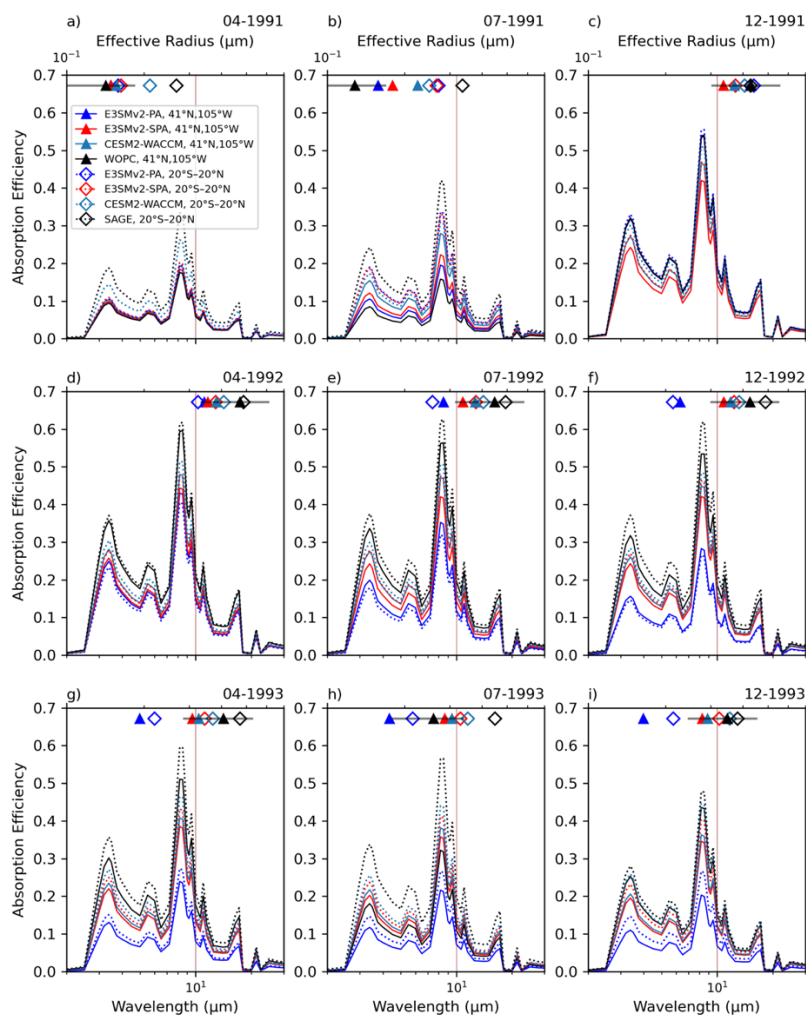
Figure 10: Monthly stratosphere absorption efficiency (Q_a) using effective size parameter ($x_{eff} = 2pR_{eff}/\lambda$) and sulfate refractive index at 0% relative humidity (Hess et al., 1998). Monthly R_{eff} are from E3SMv2-PA, E3SMv2-SPA, CESM2-WAACCM, WOPC, and SAGE-II from Fig. 3c-d, and are marked by colored triangles (41°N 105°W; WOPC) and hollow diamonds (20°S–20°N; SAGE-II) at the top of the plot. The bottom x-axis is wavelength (λ; 3–40 μm. The top axis is R_{eff} (0.1-0.7 μm) used in the calculation of Q_a via the effective size parameter (x_{eff}). The dark red line marks the terrestrial black body wavelength of maximum irradiance (10 μm).

4.6.1 long wave heating rates

640   The absorption of outgoing longwave radiation in the stratosphere results in local heating of the aerosol layer. Figure 11 shows the normalized longwave heating rate (LWH; K day^{-1}) due only to Pinatubo aerosols over the same regions as Fig. 8 and 9. Higher initial global (Fig. 11a) and 41°N (Fig. 11b) LWH in CESM2-WACCM up to March 1992 mirrors model behavior for AOD (Fig. 9a-b). The similarity to AOD indicates a LWH dependence on aerosol absorption optical depth (AAOD; level integrated b_a (Eq. B3)) – and therefore aerosol number concentration and Q_a – in these two regions. As with

645   diffuse/direct radiation (Section 4.5.1), characterizing the stratospheric longwave heating rate based solely on Q_a (i.e., aerosol size) is an oversimplification of the actual stratospheric absorption because number concentration is also acting to scale the b_a.

        The E3SMv2-presc has no Pinatubo signal in LWH. This is related to how the prescribed volcanic forcing is treated in the model and is not indicative of a missing physical mechanism. While a select number of diagnostics include contributions from the GLoSSAC forcing dataset (e.g., AOD, radiation flux, SSA), LWH does not.
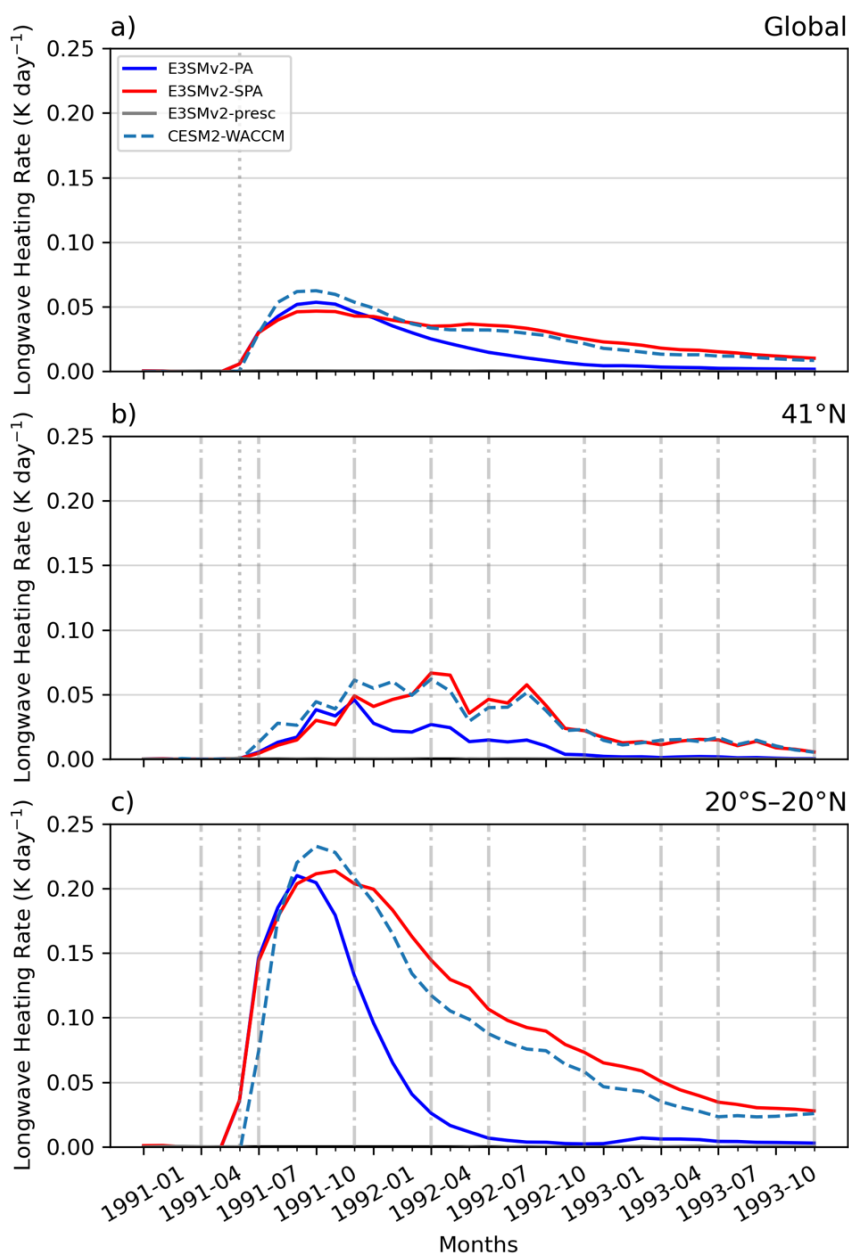
Figure 11: Pinatubo induced changes in longwave heating rate (K day⁻¹) over the modeled longwave wavebands (waveband midpoints of ~3.5-514 μm) (Neale et al., 2012). Regions include global stratospheric mean (a), a midlatitude band stratospheric mean at WOPC pressure levels (b; 41°N, 130-10 hPa), and a tropical band stratospheric mean at SAGE-II pressure levels (c; 20°S-20°N, 50-10 hPa). The Pinatubo eruption is marked with the gray dotted line at 1991-06, and the sample months for Fig. 7 are marked

650

5. Discussion

The preceding sections present encouraging results for E3SMv2-SPA and its ability to model explosive volcanic eruptions. These results begin at the global scale and move into the micro-scale, tying the latter to the former to understand the

660   strengths and weaknesses of the modal aerosol modeling approach. While this stratospheric parameterization is new to E3SM, it is based on a modeling framework developed for CESM2-WACCM which has an additional interactive chemistry element not present in E3SM (Mills et al., 2016). Along with the variety of observational datasets, E3SMv2-SPA is validated against CESM2-WACCM which elucidates the effects of interactive chemistry on aerosol formation.

On the global scale, E3SMv2-SPA performs well compared to observational datasets and has similar behavior to

665   CESM2-WACCM. The near-globally averaged stratospheric sulfate burden in E3SMv2-SPA agrees well with SAGE-3l and HIRS remote sensing datasets (Fig. 1), indicating that the model does a reasonable job of simulating aerosol lifetime and loading in the stratosphere. The higher mass burdens in E3SMv2-SPA than in CESM2-WACCM point to the OH consumption in CESM2-WACCM's interactive chemistry limiting aerosol formation from SO_2. For near-global AOD, the volcanically parameterized E3SMv2-SPA, CESM2-WACCM, and E3SMv2-presc all have similar performance and all exhibit a similar

670   shape to the retrieved AVHRR AOD (Fig. 2). The models underestimate AOD compared to AVHRR in the 15 months following the eruption, but then agree well with AVHRR to the end of 1993. An aspect of the initial eruption that is left out of the models is the injection of large volcanic ash particles, and this may partly explain the low AOD bias shortly after the eruption. However, these particles are short lived (~3 days (Guo et al., 2004a)), and the likely culprits for the AOD underestimation are aerosol number and size representation.

675   The modelled aerosol size – represented by R_{eff} – is consistently underestimated compared to both in-situ and remote sensing datasets (Fig. 3). E3SMv2-SPA has slightly smaller R_{eff} than CESM2-WACCM, where the slightly larger aerosols are attributed to fewer initial Aitken mode aerosol associated with the limited OH oxidation in CESM2-WACCM. Unpacking R_{eff} into its component modal distributions on a global scale illustrates the larger modal D_g and also smaller modal numer concentration in CESM2-WACCM (Fig. 4). While useful for visualizing the evolution of a variety of volcanic eruptions over

680   this period, validation with observations requires the finer-scale comparison of model and in-situ data.

The comparisons with balloon-borne WOPC data (Fig. 5) identify a key reason for the underestimation in R_{eff}. Namely, that modelled coarse mode aerosols are not big enough in the models during the first year after Pinatubo. The aerosol modes reach a similar pattern of change after a year and there is very close agreement in the microphysics of E3SMv2-SPA and CESM2-WACCM. The inability to create large enough aerosol in the models can affect the simulated climate impacts,

685   and the size-based effects on scattering and absorption are explored through the single particle Mie scattering.

The plotted Q_s (Fig. 6,7) and Q_a (Fig. 10) tell an idealized story about how size affects scattering of incoming solar and absorption of outgoing terrestrial radiation. At the wavelength of peak incoming solar irradiance (0.5 μm; l_{solar}), the larger

observed aerosols manifest as weaker scatterers of incident radiation than E3SMv2-SPA and CESM2-WACCM. This indicates that the models may overestimate aerosol scattering, though the differences between model and observation are smaller for

690 monthly as opposed to daily averages. For Q_a, the relationship is simpler, with a linear increase in aerosol absorption with increasing aerosol size. Our results show that the models may underestimate absorption of light at the wavelength of peak outgoing terrestrial radiation (10 µm; l_{earth}) due to their smaller simulated aerosol size. When the effects of modeled interstitial aerosol water are included in the CESM2-WACCM refractive index, modeled Q_a is decreased further when compared to observations due to a lower absorption of l_{earth} by water than by sulfate.

695 Care should be taken in interpreting Q_s and Q_a as there are some caveats to the above comparisons. While effective radius is a reasonable representation of aerosol size and is an important factor in aerosol optics, it is not the singular factor in aerosol optical properties. Aerosol number is neglected in these comparisons, which is a secondary determiner to aerosol AOD. The importance of aerosol number can be seen in the diffuse radiation (Fig. 8), which has relative model behaviors that mirror those of AOD (Fig. 9). Number is also important in longwave absorption, where relative modeled longwave heating rates (Fig.

700 11) similarly mirror those in AOD. Another assumption in the calculation of scattering and absorption efficiencies is the assumption of a stratospheric sulfate refractive index. This is consistently done for remote sensing datasets where no additional information can be provided, but in models that prognostically calculate the volume-weighted soluble refractive index this may be misleading. Here, the same refractive index is assumed across observations and models to make them more comparable. It also avoids differences in CESM2-WACCM and E3SM that arise from the extremely low stratospheric water bias in E3SM.

705 The accurate simulation of number and refractive index are two aspects of this work that require further study.

This study has served to validate the stratospheric prognostic aerosol treatment in E3SMv2-SPA against observations, while also showing it can have reasonable performance compared to the more comprehensive chemical treatment of CESM2-WACCM. We have connected the microphysical evolution of aerosols to radiative impacts, which then cascade into further downstream impacts (i.e., changes in temperature, precipitation, water vapor, etc.) that will be explored in follow-on papers.

710 While an interactive chemical treatment does have better overall agreement with observations of mass burden, AOD, and R_{eff}, E3SMv2-SPA can still serve as a viable alternative. Hence, E3SMv2-SPA will enable studies of climate impacts from stratospheric aerosols with varied source characteristics in free-running fully-coupled climate simulations.

Appendix A: Effective radius

Aerosol effective radius (R_{eff}) – or area-weighted aerosol radius – is a good representation of a size distribution's

715 optically relevant size (Hansen and Travis, 1974; Russell et al., 1996). This relies on the fact that intercepted light is proportional to the particle radius in Mie and geometric scattering regimes. These regimes can be designated by an aerosol size parameter, $x = \frac{2\pi r}{wavlength\ (\lambda)}$, with Mie scattering corresponding to $x \approx 0.2 - 2000$ and geometric scattering corresponding to $x > 2000$ (Petty, 2006). R_{eff} is calculated by taking the ratio of the third aerosol moment (volume) and second aerosol moment (cross-sectional area) (M_3 and M_2, respectively) of the aerosol size distribution (Hansen and Travis, 1974):

720

$$R_{eff} = \frac{M_3}{M_2},$$

(1)

A lognormal size distribution is defined as

725 $$n_N(\ln r) = \frac{dN(r)}{d \ln r} = \frac{N}{\ln \sigma_g \sqrt{2\pi}} e^{\left[-\frac{1}{2}\left(\frac{\ln r - \ln r_g}{\ln \sigma_g}\right)^2\right]},$$

(2)

where N is total aerosol number concentration, r_g is the wet geometric mean radius, r is the radius, and s_g is the geometric standard deviation. The analytic expression for the aerosol moments, M_n, of a lognormal distribution are,

730 $$M_n = N r_g^n e^{\left[\frac{n^2}{2}(\ln \sigma_g)^2\right]},$$

(3)

For a multimodal system, the modal moments ($M_{n,i}$) can be summed, giving the final equation for R_{eff}:

$$R_{eff} = \frac{\sum_{i=1}^m M_{3,i}}{\sum_{i=1}^m M_{2,i}} = \frac{\sum_{i=1}^m N_i r_{g,i}^3 e^{\left[\frac{9}{2} \ln \sigma_{g,i}^2\right]}}{\sum_{i=1}^m N_i r_{g,i}^2 e^{\left[2 \ln \sigma_{g,i}^2\right]}},$$

(4)

735

Appendix B: Single-particle Mie scattering

In order to understand how improvements to stratospheric aerosol size distributions affect simulated climate impact, aerosol scattering and absorption efficiencies (Q_s, Q_a) are calculated based on Mie theory, the solution of Maxwell's equations for the interaction of radiation with a sphere (Hansen and Travis, 1974). The Q_s (Q_a) is the surface area of the shadow cast by

740 the particle due to scattering (absorption) of intercepted light divided by the geometric cross section (πr^2). Q_s and Q_a are calculated using the python package, miepython (https://miepython.readthedocs.io/en/latest/index.html#). This package simulates absorption and scattering of incident light by non-absorbing or partially absorbing spheres and requires a complex aerosol refractive index ($n = a + bi$) and aerosol size parameter (aerosol circumference over the incident wavelength of light) as inputs. In the complex refractive index, the real and imaginary parts define scattering and absorption, respectively. Here, an

745 effective size parameter is used as a proxy for the particle size distributions in our calculations:

$$x_{eff} = \frac{2\pi R_{eff}}{\lambda},$$

(1)

We note that because Mie theory calculates these values based on interactions with a single sphere and we are using the
number-independent R_{eff} as an input, Q_s and Q_a do not account for effects of different number concentrations. The volume
scattering and absorption coefficients (β_s, β_a; units of m^{-1}) do include the effect of aerosol number, but are not generated based
on our comparisons due to the ambiguity of assuming an effective aerosol number. Their equations are included below for
completeness.

$$\beta_s = N Q_s \pi r^2 , \tag{2}$$
$$\beta_a = N Q_a \pi r^2 , \tag{3}$$

The aerosol refractive index in the models is derived from a combination of sulfate aerosol and water due to the prevalence of
sulfate in the stratosphere following Pinatubo. Because sulfate is a soluble species, a soluble refractive index (n_s) can be
calculated with the volume mixing rule (Ghan and Zaveri, 2007):

$$n_s = \frac{1}{V_s}\left(\frac{n_{wat} m_{wat}}{\rho_{wat}} + \frac{n_{sulf} m_{sulf}}{\rho_{sulf}}\right), \tag{4}$$

where n_{wat}, m_{wat}, and r_{wat} are the water complex refractive index, aerosol water mass (kg), and water density (kg m^{-3}); and n_{sulf},
m_{sulf}, and r_{sulf} are the sulfate complex refractive index, sulfate mass (kg), and sulfate density (kg m^{-3}). The soluble aerosol
volume across modes (V_s) is calculated from the volume mean radius (R_{eff}):

$$V_s = \frac{4}{3}\pi R_{eff}^3, \tag{5}$$

Sulfate and water refractive indices are taken from the literature (Hess et al., 1998; Hale and Querry, 1973). The sulfate
refractive index reported in Hess et al. (1998) (n_{Hess}) is at 0% relative humidity and corresponds to aerosol that is approximately
25% water / 75% H$_2$SO$_4$ by mass (Seinfeld and Pandis, 2006). A similar solution ratio has been used in other remote sensing
applications (see Section 3), and for our in-situ and remote sensing datasets we assume stratospheric aerosol optical properties
are reasonably represented by n_{Hess}. The pure sulfate refractive index used in E3SM/CESM (n_{sulf}) is calculated from water and
n_{Hess} following methods in Ghan and Zaveri (2007) and is nearly identical to n_{Hess}, albeit reported at a lower wavelength
resolution. Given their similarity and the higher wavelength resolution in n_{Hess}, we use n_{Hess} instead of E3SM's pure sulfate
refractive index for model single particle scattering calculations.

6. Code Availability

All model code is publicly available on Github. The E3SMv2-SPA model code can be found at
https://github.com/sandialabs/CLDERA-E3SM; E3SMv2-PA model code can be found at https://github.com/E3SM-

Project/E3SM; CESM2-WACCM data can be found at https://github.com/ESCOMP/CESM. Plotting and processing scripts used in the analyses of this paper can be found on Figshare (https://doi.org/10.6084/m9.figshare.24844815.v1).

7. Data Availability

The WOPC balloon data are available in the data repository at the University of Wyoming Libraries (Deshler and Kalnajs, 2022). AVHRR data can be found at doi:10.25921/w3zj-4y48 (Xuepeng and NOAA CDR Progra). For SAGE, AVHRR, and some of the postprocessed WOPC data, see https://doi.org/10.7298/mm1s-ae98 (Quaglia et al., 2022) .The original 2-degree volcanic emissions file (VolcanEESMv3.11_SO2_850-2016_Mscale_Zreduc_2deg_c180812.nc) can be retrieved from https://svn-ccsm-inputdata.cgd.ucar.edu/trunk/inputdata/atm/cam/chem/stratvolc/. The raw model output data used in this paper has been archived on the DOE NERSC resources and is available upon request.

8. Author Contribution

Conceptualization: Hunter Brown, Benjamin Wagman, Diana Bull, Kara Peterson, Xiaohong Liu, Ziming Ke; **Data curation:** Hunter Brown, Benjamin Wagman, Benjamin Hillman, Ziming Ke, Lin Lin; **Formal analysis**: Hunter Brown; **Funding acquisition**: Diana Bull, Kara Peterson; **Investigation:** Hunter Brown; **Methodology**: Hunter Brown, Benjamin Wagman, Diana Bull, Xiaohong Liu, Ziming Ke, Lin Lin; **Project administration:** Diana Bull, Kara Peterson; **Resources**: Diana Bull, Kara Peterson; **Software**: Hunter Brown, Ben Hillman, Ziming Ke, Lin Lin; **Supervision**: Diana Bull, Kara Peterson, Benjamin Wagman; **Validation**: Hunter Brown; **Visualization**: Hunter Brown; **Writing – original draft preparation**: Hunter Brown, Diana Bull, Kara Peterson, Benjamin Wagman; **Writing – review & editing**: All authors.

9. Competing interests

At least one of the (co-)authors is a member of the editorial board of Geoscientific Model Development.

10. Acknowledgements

We would like to acknowledge Terry Deshler and Lars Kalnajs for providing access to the WOPC balloon data and helping with questions that arose. Po-Lun Ma provided 6-hourly MERRA2 nudging data. Processing the MERRA-2 reanalysis for nudging E3SM was supported by the Enabling Aerosol-cloud interactions at Global convection-permitting scalES (EAGLES) project (project no 74358), funded by the U.S. Department of Energy, Office of Science, Office of Biological and Environmental Research, Earth System Model Development program area. Thanks to Ilaria Quaglia for access to processed AVHRR, SAGE, WOPC data. This research used resources of the National Energy Research Scientific Computing Center (NERSC), a U.S. Department of Energy Office of Science User Facility located at Lawrence Berkeley National Laboratory, operated under Contract No. DE-AC02-05CH11231 using NERSC award BER-ERCAP0022865. This work was supported by the Laboratory Directed Research and Development program at Sandia National Laboratories, a multimission laboratory managed and operated by National Technology and Engineering Solutions of Sandia LLC, a wholly owned subsidiary of

Honeywell International Inc. for the U.S. Department of Energy's National Nuclear Security Administration under contract DE-NA0003525. SAND2023-XXXX.

References

Baran, A. J. and Foot, J. S.: New application of the operational sounder HIRS in determining a climatology of sulphuric acid

815   aerosol from the Pinatubo eruption, J. Geophys. Res., 99, 25673, https://doi.org/10.1029/94JD02044, 1994.

Borbas, E. E. and Menzel, P. W.: Observed HIRS and Aqua MODIS Thermal Infrared Moisture Determinations in the 2000s, Remote Sensing, 13, 502, https://doi.org/10.3390/rs13030502, 2021.

Church, J. A., White, N. J., and Arblaster, J. M.: Significant decadal-scale impact of volcanic eruptions on sea level and ocean heat content, Nature, 438, 74–77, https://doi.org/10.1038/nature04237, 2005.

820   Damadeo, R. P., Zawodny, J. M., Thomason, L. W., and Iyer, N.: SAGE version 7.0 algorithm: application to SAGE II, Atmos. Meas. Tech., 6, 3539–3561, https://doi.org/10.5194/amt-6-3539-2013, 2013.

Danabasoglu, G., Lamarque, J. -F., Bacmeister, J., Bailey, D. A., DuVivier, A. K., Edwards, J., Emmons, L. K., Fasullo, J., Garcia, R., Gettelman, A., Hannay, C., Holland, M. M., Large, W. G., Lauritzen, P. H., Lawrence, D. M., Lenaerts, J. T. M., Lindsay, K., Lipscomb, W. H., Mills, M. J., Neale, R., Oleson, K. W., Otto-Bliesner, B., Phillips, A. S., Sacks, W., Tilmes, S.,

825   Kampenhout, L., Vertenstein, M., Bertini, A., Dennis, J., Deser, C., Fischer, C., Fox-Kemper, B., Kay, J. E., Kinnison, D., Kushner, P. J., Larson, V. E., Long, M. C., Mickelson, S., Moore, J. K., Nienhouse, E., Polvani, L., Rasch, P. J., and Strand, W. G.: The Community Earth System Model Version 2 (CESM2), J. Adv. Model. Earth Syst., 12, https://doi.org/10.1029/2019MS001916, 2020.

Deshler, T.: In situ measurements of Pinatubo aerosol over Kiruna on four days between 18 January and 13 February 1992,

830   Geophys. Res. Lett., 21, 1323–1326, https://doi.org/10.1029/93GL03227, 1994.

Deshler, T.: Thirty years of in situ stratospheric aerosol size distribution measurements from Laramie, Wyoming (41°N), using balloon-borne instruments, J. Geophys. Res., 108, 4167, https://doi.org/10.1029/2002JD002514, 2003.

Deshler, T. and Kalnajs, L. E.: University of Wyoming stratospheric aerosol measurements | Mid latitudes, https://doi.org/10.15786/21534894, 2022.

835   Deshler, T., Hofmann, D. J., Johnson, B. J., and Rozier, W. R.: Balloonborne measurements of the Pinatubo aerosol size distribution and volatility at Laramie, Wyoming during the summer of 1991, Geophys. Res. Lett., 19, 199–202, https://doi.org/10.1029/91GL02787, 1992.

Deshler, T., Johnson, B. J., and Rozier, W. R.: Balloonborne measurements of Pinatubo aerosol during 1991 and 1992 at 41°N: Vertical profiles, size distribution, and volatility, Geophys. Res. Lett., 20, 1435–1438, https://doi.org/10.1029/93GL01337,

840   1993.

Deshler, T., Luo, B., Kovilakam, M., Peter, T., and Kalnajs, L. E.: Retrieval of Aerosol Size Distributions From In Situ Particle Counter Measurements: Instrument Counting Efficiency and Comparisons With Satellite Measurements, J. Geophys. Res. Atmos., 124, 5058–5087, https://doi.org/10.1029/2018JD029558, 2019.

Dunne, J. P., Horowitz, L. W., Adcroft, A. J., Ginoux, P., Held, I. M., John, J. G., Krasting, J. P., Malyshev, S., Naik, V.,
845 Paulot, F., Shevliakova, E., Stock, C. A., Zadeh, N., Balaji, V., Blanton, C., Dunne, K. A., Dupuis, C., Durachta, J., Dussin, R., Gauthier, P. P. G., Griffies, S. M., Guo, H., Hallberg, R. W., Harrison, M., He, J., Hurlin, W., McHugh, C., Menzel, R., Milly, P. C. D., Nikonov, S., Paynter, D. J., Ploshay, J., Radhakrishnan, A., Rand, K., Reichl, B. G., Robinson, T., Schwarzkopf, D. M., Sentman, L. T., Underwood, S., Vahlenkamp, H., Winton, M., Wittenberg, A. T., Wyman, B., Zeng, Y., and Zhao, M.: The GFDL Earth System Model Version 4.1 (GFDL-ESM 4.1): Overall Coupled Model Description and
850 Simulation Characteristics, J Adv Model Earth Syst, 12, e2019MS002015, https://doi.org/10.1029/2019MS002015, 2020.

Dykema, J. A., Keith, D. W., and Keutsch, F. N.: Improved aerosol radiative properties as a foundation for solar geoengineering risk assessment, Geophys. Res. Lett., 43, 7758–7766, https://doi.org/10.1002/2016GL069258, 2016.

English, J. M., Toon, O. B., and Mills, M. J.: Microphysical simulations of large volcanic eruptions: Pinatubo and Toba: MICROPHYSICS OF PINATUBO/TOBA ERUPTIONS, J. Geophys. Res. Atmos., 118, 1880–1895,
855 https://doi.org/10.1002/jgrd.50196, 2013.

Gao, C. Y., Naik, V., Horowitz, L. W., Ginoux, P., Paulot, F., Dunne, J., Mills, M., Aquila, V., and Colarco, P.: Volcanic Drivers of Stratospheric Sulfur in GFDL ESM4, J Adv Model Earth Syst, 15, e2022MS003532, https://doi.org/10.1029/2022MS003532, 2023.

Garcia, R. R., Marsh, D. R., Kinnison, D. E., Boville, B. A., and Sassi, F.: Simulation of secular trends in the middle
860 atmosphere, 1950–2003, J. Geophys. Res., 112, D09301, https://doi.org/10.1029/2006JD007485, 2007.

Gettelman, A. and Morrison, H.: Advanced Two-Moment Bulk Microphysics for Global Models. Part I: Off-Line Tests and Comparison with Other Schemes, Journal of Climate, 28, 1268–1287, https://doi.org/10.1175/JCLI-D-14-00102.1, 2015.

Gettelman, A., Mills, M. J., Kinnison, D. E., Garcia, R. R., Smith, A. K., Marsh, D. R., Tilmes, S., Vitt, F., Bardeen, C. G., McInerny, J., Liu, H. -L., Solomon, S. C., Polvani, L. M., Emmons, L. K., Lamarque, J. -F., Richter, J. H., Glanville, A. S.,
865 Bacmeister, J. T., Phillips, A. S., Neale, R. B., Simpson, I. R., DuVivier, A. K., Hodzic, A., and Randel, W. J.: The Whole Atmosphere Community Climate Model Version 6 (WACCM6), JGR Atmospheres, 124, 12380–12403, https://doi.org/10.1029/2019JD030943, 2019.

Ghan, S. J. and Zaveri, R. A.: Parameterization of optical properties for hydrated internally mixed aerosol, Journal of Geophysical Research, 112, https://doi.org/10.1029/2006JD007927, 2007.

870 Gillett, N. P., Weaver, A. J., Zwiers, F. W., and Wehner, M. F.: Detection of volcanic influence on global precipitation: VOLCANIC INFLUENCE ON PRECIPITATION, Geophys. Res. Lett., 31, n/a-n/a, https://doi.org/10.1029/2004GL020044, 2004.

Golaz, J., Van Roekel, L. P., Zheng, X., Roberts, A. F., Wolfe, J. D., Lin, W., Bradley, A. M., Tang, Q., Maltrud, M. E., Forsyth, R. M., Zhang, C., Zhou, T., Zhang, K., Zender, C. S., Wu, M., Wang, H., Turner, A. K., Singh, B., Richter, J. H., Qin,

875   Y., Petersen, M. R., Mametjanov, A., Ma, P., Larson, V. E., Krishna, J., Keen, N. D., Jeffery, N., Hunke, E. C., Hannah, W. M., Guba, O., Griffin, B. M., Feng, Y., Engwirda, D., Di Vittorio, A. V., Dang, C., Conlon, L. M., Chen, C., Brunke, M. A., Bisht, G., Benedict, J. J., Asay-Davis, X. S., Zhang, Y., Zhang, M., Zeng, X., Xie, S., Wolfram, P. J., Vo, T., Veneziani, M., Tesfa, T. K., Sreepathi, S., Salinger, A. G., Reeves Eyre, J. E. J., Prather, M. J., Mahajan, S., Li, Q., Jones, P. W., Jacob, R. L., Huebler, G. W., Huang, X., Hillman, B. R., Harrop, B. E., Foucar, J. G., Fang, Y., Comeau, D. S., Caldwell, P. M.,

880   Bartoletti, T., Balaguru, K., Taylor, M. A., McCoy, R. B., Leung, L. R., and Bader, D. C.: The DOE E3SM Model Version 2: Overview of the Physical Model and Initial Model Evaluation, J Adv Model Earth Syst, 14, https://doi.org/10.1029/2022MS003156, 2022.

Grainger, R. G., Lambert, A., Rodgers, C. D., Taylor, F. W., and Deshler, T.: Stratospheric aerosol effective radius, surface area and volume estimated from infrared measurements, J. Geophys. Res., 100, 16507, https://doi.org/10.1029/95JD00988,

885   1995.

Greenwald, R., Bergin, M. H., Xu, J., Cohan, D., Hoogenboom, G., and Chameides, W. L.: The influence of aerosols on crop production: A study using the CERES crop model, Agricultural Systems, 89, 390–413, https://doi.org/10.1016/j.agsy.2005.10.004, 2006.

Gu, L., Baldocchi, D. D., Wofsy, S. C., Munger, J. W., Michalsky, J. J., Urbanski, S. P., and Boden, T. A.: Response of a

890   Deciduous Forest to the Mount Pinatubo Eruption: Enhanced Photosynthesis, Science, 299, 2035–2038, https://doi.org/10.1126/science.1078366, 2003.

Guo, S., Rose, W. I., Bluth, G. J. S., and Watson, I. M.: Particles in the great Pinatubo volcanic cloud of June 1991: The role of ice, Geochem. Geophys. Geosyst., 5, n/a-n/a, https://doi.org/10.1029/2003GC000655, 2004a.

Guo, S., Bluth, G. J. S., Rose, W. I., Watson, I. M., and Prata, A. J.: Re-evaluation of SO2 release of the 15 June 1991 Pinatubo

895   eruption using ultraviolet and infrared satellite sensors, Geochem. Geophys. Geosyst., 5, n/a-n/a, https://doi.org/10.1029/2003GC000654, 2004b.

Hale, G. M. and Querry, M. R.: Optical Constants of Water in the 200-nm to 200-μm Wavelength Region, Appl. Opt., 12, 555, https://doi.org/10.1364/AO.12.000555, 1973.

Hansen, J. E. and Travis, L. D.: Light scattering in planetary atmospheres, Space Sci Rev, 16, 527–610,

900   https://doi.org/10.1007/BF00168069, 1974.

Heidinger, A. K., Foster, M. J., Walther, A., and Zhao, X. (Tom): The Pathfinder Atmospheres–Extended AVHRR Climate Dataset, Bull. Amer. Meteor. Soc., 95, 909–922, https://doi.org/10.1175/BAMS-D-12-00246.1, 2014.

Hess, M., Koepke, P., and Schult, I.: Optical Properties of Aerosols and Clouds: The Software Package OPAC, Bulletin of the American Meteorological Society, 79, 831–844, https://doi.org/10.1175/1520-0477(1998)079<0831:OPOAAC>2.0.CO;2,

905   1998.

Hofmann, D. J., Oltmans, S. J., Lathrop, J. A., Harris, J. M., and Vömel, H.: Record low ozone at the South Pole in the spring of 1993, Geophys. Res. Lett., 21, 421–424, https://doi.org/10.1029/94GL00309, 1994.

Hoose, C., Kristjánsson, J. E., Chen, J.-P., and Hazra, A.: A Classical-Theory-Based Parameterization of Heterogeneous Ice Nucleation by Mineral Dust, Soot, and Biological Particles in a Global Climate Model, Journal of the Atmospheric Sciences, 910 67, 2483–2503, https://doi.org/10.1175/2010JAS3425.1, 2010.

Hsu, J. and Prather, M. J.: Stratospheric variability and tropospheric ozone, J. Geophys. Res., 114, D06102, https://doi.org/10.1029/2008JD010942, 2009.

Hurrell, J. W., Holland, M. M., Gent, P. R., Ghan, S., Kay, J. E., Kushner, P. J., Lamarque, J.-F., Large, W. G., Lawrence, D., Lindsay, K., Lipscomb, W. H., Long, M. C., Mahowald, N., Marsh, D. R., Neale, R. B., Rasch, P., Vavrus, S., Vertenstein, 915 M., Bader, D., Collins, W. D., Hack, J. J., Kiehl, J., and Marshall, S.: The Community Earth System Model: A Framework for Collaborative Research, Bull. Amer. Meteor. Soc., 94, 1339–1360, https://doi.org/10.1175/BAMS-D-12-00121.1, 2013.

Iacono, M. J., Delamere, J. S., Mlawer, E. J., Shephard, M. W., Clough, S. A., and Collins, W. D.: Radiative forcing by long-lived greenhouse gases: Calculations with the AER radiative transfer models, J. Geophys. Res., 113, D13103, https://doi.org/10.1029/2008JD009944, 2008.

920 Ivy, D. J., Solomon, S., Kinnison, D., Mills, M. J., Schmidt, A., and Neely, R. R.: The influence of the Calbuco eruption on the 2015 Antarctic ozone hole in a fully coupled chemistry-climate model, Geophysical Research Letters, 44, 2556–2561, https://doi.org/10.1002/2016GL071925, 2017.

Kalnajs, L. E. and Deshler, T.: A New Instrument for Balloon-Borne *In Situ* Aerosol Size Distribution Measurements, the Continuation of a 50 Year Record of Stratospheric Aerosols Measurements, JGR Atmospheres, 127, 925 https://doi.org/10.1029/2022JD037485, 2022.

Keeble, J., Hassler, B., Banerjee, A., Checa-Garcia, R., Chiodo, G., Davis, S., Eyring, V., Griffiths, P. T., Morgenstern, O., Nowack, P., Zeng, G., Zhang, J., Bodeker, G., Burrows, S., Cameron-Smith, P., Cugnet, D., Danek, C., Deushi, M., Horowitz, L. W., Kubin, A., Li, L., Lohmann, G., Michou, M., Mills, M. J., Nabat, P., Olivié, D., Park, S., Seland, Ø., Stoll, J., Wieners, K.-H., and Wu, T.: Evaluating stratospheric ozone and water vapour changes in CMIP6 models from 1850 to 2100, Atmos. 930 Chem. Phys., 21, 5015–5061, https://doi.org/10.5194/acp-21-5015-2021, 2021.

Kinne, S., Toon, O. B., and Prather, M. J.: Buffering of stratospheric circulation by changing amounts of tropical ozone a Pinatubo Case Study, Geophys. Res. Lett., 19, 1927–1930, https://doi.org/10.1029/92GL01937, 1992.

Kovilakam, M., Thomason, L. W., Ernest, N., Rieger, L., Bourassa, A., and Millán, L.: The Global Space-based Stratospheric Aerosol Climatology (version 2.0): 1979–2018, Earth Syst. Sci. Data, 12, 2607–2634, https://doi.org/10.5194/essd-12-2607- 935 2020, 2020.

Kravitz, B., MacMartin, D. G., Mills, M. J., Richter, J. H., Tilmes, S., Lamarque, J., Tribbia, J. J., and Vitt, F.: First Simulations of Designing Stratospheric Sulfate Aerosol Geoengineering to Meet Multiple Simultaneous Climate Objectives, J. Geophys. Res. Atmos., 122, https://doi.org/10.1002/2017JD026874, 2017.

Kremser, S., Thomason, L. W., von Hobe, M., Hermann, M., Deshler, T., Timmreck, C., Toohey, M., Stenke, A., Schwarz, J. 940 P., Weigel, R., Fueglistaler, S., Prata, F. J., Vernier, J.-P., Schlager, H., Barnes, J. E., Antuña-Marrero, J.-C., Fairlie, D., Palm, M., Mahieu, E., Notholt, J., Rex, M., Bingen, C., Vanhellemont, F., Bourassa, A., Plane, J. M. C., Klocke, D., Carn, S. A.,

Clarisse, L., Trickl, T., Neely, R., James, A. D., Rieger, L., Wilson, J. C., and Meland, B.: Stratospheric aerosol-Observations, processes, and impact on climate: Stratospheric Aerosol, Rev. Geophys., 54, 278–335, https://doi.org/10.1002/2015RG000511, 2016.

945 Labitzke, K. and McCormick, M. P.: Stratospheric temperature increases due to Pinatubo aerosols, Geophys. Res. Lett., 19, 207–210, https://doi.org/10.1029/91GL02940, 1992.

Lacis, A., Hansen, J., and Sato, M.: Climate forcing by stratospheric aerosols, Geophys. Res. Lett., 19, 1607–1610, https://doi.org/10.1029/92GL01620, 1992.

Lambert, A., Grainger, R. G., Rodgers, C. D., Taylor, F. W., Mergenthaler, J. L., Kumer, J. B., and Massie, S. T.: Global
950 evolution of the Mt. Pinatubo volcanic aerosols observed by the infrared limb-sounding instruments CLAES and ISAMS on the Upper Atmosphere Research Satellite, J. Geophys. Res., 102, 1495–1512, https://doi.org/10.1029/96JD00096, 1997.

Larson, V. E.: CLUBB-SILHS: A parameterization of subgrid variability in the atmosphere, https://doi.org/10.48550/ARXIV.1711.03675, 2017.

Lee, K. and Chung, C. E.: Observationally-constrained estimates of global fine-mode AOD, Atmos. Chem. Phys., 13, 2907–
955 2921, https://doi.org/10.5194/acp-13-2907-2013, 2013.

Leung, L. R., Bader, D. C., Taylor, M. A., and McCoy, R. B.: An Introduction to the E3SM Special Collection: Goals, Science Drivers, Development, and Analysis, J. Adv. Model. Earth Syst., 12, https://doi.org/10.1029/2019MS001821, 2020.

Liu, X. and Penner, J. E.: Effect of Mount Pinatubo H_2SO_4 / H_2O aerosol on ice nucleation in the upper troposphere using a global chemistry and transport model, J. Geophys. Res., 107, 4141, https://doi.org/10.1029/2001JD000455, 2002.

960 Liu, X., Easter, R. C., Ghan, S. J., Zaveri, R., Rasch, P., Shi, X., Lamarque, J.-F., Gettelman, A., Morrison, H., Vitt, F., Conley, A., Park, S., Neale, R., Hannay, C., Ekman, A. M. L., Hess, P., Mahowald, N., Collins, W., Iacono, M. J., Bretherton, C. S., Flanner, M. G., and Mitchell, D.: Toward a minimal representation of aerosols in climate models: description and evaluation in the Community Atmosphere Model CAM5, Geoscientific Model Development, 5, 709–739, https://doi.org/10.5194/gmd-5-709-2012, 2012.

965 Liu, X., Ma, P.-L., Wang, H., Tilmes, S., Singh, B., Easter, R. C., Ghan, S. J., and Rasch, P. J.: Description and evaluation of a new four-mode version of the Modal Aerosol Module (MAM4) within version 5.3 of the Community Atmosphere Model, Geoscientific Model Development, 9, 505–522, https://doi.org/10.5194/gmd-9-505-2016, 2016.

Marsh, D. R., Mills, M. J., Kinnison, D. E., Lamarque, J.-F., Calvo, N., and Polvani, L. M.: Climate Change from 1850 to 2005 Simulated in CESM1(WACCM), Journal of Climate, 26, 7372–7391, https://doi.org/10.1175/JCLI-D-12-00558.1, 2013.

970 Marshall, L., Johnson, J. S., Mann, G. W., Lee, L., Dhomse, S. S., Regayre, L., Yoshioka, M., Carslaw, K. S., and Schmidt, A.: Exploring How Eruption Source Parameters Affect Volcanic Radiative Forcing Using Statistical Emulation, J. Geophys. Res. Atmos., 124, 964–985, https://doi.org/10.1029/2018JD028675, 2019.

Mauldin, L. E., Zaun, N. H., McCormick, Jr., M. P., Guy, J. H., and Vaughn, W. R.: Stratospheric Aerosol And Gas Experiment II Instrument: A Functional Description, Opt. Eng., 24, 242307, https://doi.org/10.1117/12.7973473, 1985.

975   McCormick, M. P., Thomason, L. W., and Trepte, C. R.: Atmospheric effects of the Mt Pinatubo eruption, Nature, 373, 399–404, https://doi.org/10.1038/373399a0, 1995.

Mills, M. J., Schmidt, A., Easter, R., Solomon, S., Kinnison, D. E., Ghan, S. J., Neely, R. R., Marsh, D. R., Conley, A., Bardeen, C. G., and Gettelman, A.: Global volcanic aerosol properties derived from emissions, 1990–2014, using CESM1(WACCM), J. Geophys. Res. Atmos., 121, 2332–2348, https://doi.org/10.1002/2015JD024290, 2016.

980   Mills, M. J., Richter, J. H., Tilmes, S., Kravitz, B., MacMartin, D. G., Glanville, A. A., Tribbia, J. J., Lamarque, J., Vitt, F., Schmidt, A., Gettelman, A., Hannay, C., Bacmeister, J. T., and Kinnison, D. E.: Radiative and Chemical Response to Interactive Stratospheric Sulfate Aerosols in Fully Coupled CESM1(WACCM), J. Geophys. Res. Atmos., 122, https://doi.org/10.1002/2017JD027006, 2017.

Nagaraja Rao, C. R., Stowe, L. L., and McCLAIN, E. P.: Remote sensing of aerosols over the oceans using AVHRR data

985   Theory, practice and applications, International Journal of Remote Sensing, 10, 743–749, https://doi.org/10.1080/01431168908903915, 1989.

Neale, R. B., Chen, C., Gettelman, A., Lauritzen, P. H., Park, S., Williamson, D. L., Conley, A. J., Garcia, R., Kinnison, D., Lamarque, J.-F., Marsh, D., Mills, M., Smith, A. K., Tilmes, S., Vitt, F., Morrison, H., Cameron-Smith, P. J., Collins, W. D., Iacono, M. J., Easter, R. C., Ghan, S. J., Liu, X., Rasch, P. J., and Taylor, M. A.: Description of the NCAR Community

990   Atmosphere Model (CAM 5.0), National Center for Atmospheric Research, Boulder, Colorado, USA, 2012.

Neely III, R. R. and Schmidt, A.: VolcanEESM: Global volcanic sulphur dioxide (SO2) emissions database from 1850 to present - Version 1.0 (1.0), https://doi.org/10.5285/76EBDC0B-0EED-4F70-B89E-55E606BCD568, 2016.

Parker, D. E., Wilson, H., Jones, P. D., Christy, J. R., and Folland, C. K.: The Impact of Mount Pinatubo on World-Wide Temperatures, Int. J. Climatol., 16, 487–497, https://doi.org/10.1002/(SICI)1097-0088(199605)16:5<487::AID-

995   JOC39>3.0.CO;2-J, 1996.

Petty, G.: A First Course in Atmospheric Radiation, Second Edition., Sundog Publishing, 459 pp., 2006.

Portmann, R. W., Solomon, S., Garcia, R. R., Thomason, L. W., Poole, L. R., and McCormick, M. P.: Role of aerosol variations in anthropogenic ozone depletion in the polar regions, J. Geophys. Res., 101, 22991–23006, https://doi.org/10.1029/96JD02608, 1996.

1000   Proctor, J., Hsiang, S., Burney, J., Burke, M., and Schlenker, W.: Estimating global agricultural effects of geoengineering using volcanic eruptions, Nature, 560, 480–483, https://doi.org/10.1038/s41586-018-0417-3, 2018.

Quaglia, I., Niemeier, U., Visioni, D., Pitari, G., Brühl, C., Dhomse, S. S., Franke, H., Laakso, A., Mann, G. W., Rozanov, E., and Sukhodolov, T.: Data from: Interactive Stratospheric Aerosol moels resonse to different amount and altitude of SO2 injections during teh 1991 Pinatubo eruption, https://doi.org/10.7298/mm1s-ae98, 2022.

1005   Quaglia, I., Timmreck, C., Niemeier, U., Visioni, D., Pitari, G., Brodowsky, C., Brühl, C., Dhomse, S. S., Franke, H., Laakso, A., Mann, G. W., Rozanov, E., and Sukhodolov, T.: Interactive stratospheric aerosol models' response to different amounts and altitudes of SO_2 injection during the 1991 Pinatubo eruption, Atmos. Chem. Phys., 23, 921–948, https://doi.org/10.5194/acp-23-921-2023, 2023.

Revell, L. E., Stenke, A., Luo, B., Kremser, S., Rozanov, E., Sukhodolov, T., and Peter, T.: Impacts of Mt Pinatubo volcanic
aerosol on the tropical stratosphere in chemistry–climate model simulations using CCMI and CMIP6 stratospheric aerosol
data, Atmos. Chem. Phys., 17, 13139–13150, https://doi.org/10.5194/acp-17-13139-2017, 2017.

Ridley, D. A., Heald, C. L., Kok, J. F., and Zhao, C.: An observationally constrained estimate of global dust aerosol optical
depth, Atmos. Chem. Phys., 16, 15097–15117, https://doi.org/10.5194/acp-16-15097-2016, 2016.

Robock, A.: Volcanic eruptions and climate, Rev. Geophys., 38, 191–219, https://doi.org/10.1029/1998RG000054, 2000.

Russell, P. B., Livingston, J. M., Pueschel, R. F., Bauman, J. J., Pollack, J. B., Brooks, S. L., Hamill, P., Thomason, L. W.,
Stowe, L. L., Deshler, T., Dutton, E. G., and Bergstrom, R. W.: Global to microscale evolution of the Pinatubo volcanic aerosol
derived from diverse measurements and analyses, J. Geophys. Res., 101, 18745–18763, https://doi.org/10.1029/96JD01162,
1996.

Seinfeld, J. H. and Pandis, S. N.: Atmospheric Chemistry and Physics, Second., John Wiley and Sons, Inc., 1203 pp., 2006.

Soden, B. J., Wetherald, R. T., Stenchikov, G. L., and Robock, A.: Global Cooling After the Eruption of Mount Pinatubo: A
Test of Climate Feedback by Water Vapor, Science, 296, 727–730, https://doi.org/10.1126/science.296.5568.727, 2002.

Solomon, S., Sanders, R. W., Garcia, R. R., and Keys, J. G.: Increased chlorine dioxide over Antarctica caused by volcanic
aerosols from Mount Pinatubo, Nature, 363, 245–248, https://doi.org/10.1038/363245a0, 1993.

Solomon, S., Ivy, D. J., Kinnison, D., Mills, M. J., Neely, R. R., and Schmidt, A.: Emergence of healing in the Antarctic ozone
layer, Science, 353, 269–274, https://doi.org/10.1126/science.aae0061, 2016.

Stenchikov, G. L., Kirchner, I., Robock, A., Graf, H.-F., Antuña, J. C., Grainger, R. G., Lambert, A., and Thomason, L.:
Radiative forcing from the 1991 Mount Pinatubo volcanic eruption, J. Geophys. Res., 103, 13837–13857,
https://doi.org/10.1029/98JD00693, 1998.

Tang, Q., Prather, M. J., Hsu, J., Ruiz, D. J., Cameron-Smith, P. J., Xie, S., and Golaz, J.-C.: Evaluation of the interactive
stratospheric ozone (O3v2) module in the E3SM version 1 Earth system model, Geosci. Model Dev., 14, 1219–1236,
https://doi.org/10.5194/gmd-14-1219-2021, 2021.

Taylor, F. W., other, and other: UARS Improved Stratospheric and Mesospheric Sounder (ISAMS) Level 3AT V010 (010),
1994.

Taylor, K. E., Williamson, D., and Zwiers, F.: Report 60: The sea surface temperature and sea ice concentration boundary
conditions for AMIP II simulations, Laurence Livermore National Laboratory, 28, 2000.

Thomason, L. W., Ernest, N., Millán, L., Rieger, L., Bourassa, A., Vernier, J.-P., Manney, G., Luo, B., Arfeuille, F., and Peter,
T.: A global space-based stratospheric aerosol climatology: 1979–2016, Earth Syst. Sci. Data, 10, 469–492,
https://doi.org/10.5194/essd-10-469-2018, 2018.

Timmreck, C., Graf, H., and Kirchner, I.: A one and half year interactive MA/ECHAM4 simulation of Mount Pinatubo Aerosol,
J. Geophys. Res., 104, 9337–9359, https://doi.org/10.1029/1999JD900088, 1999a.

Timmreck, C., Graf, H.-F., and Feichter, J.: Simulation of Mt. Pinatubo Volcanic Aerosol with the Hamburg Climate Model
ECHAM4, Theoretical and Applied Climatology, 62, 85–108, https://doi.org/10.1007/s007040050076, 1999b.

Toon, O. B., Turco, R. P., Westphal, D., Malone, R., and Liu, M.: A Multidimensional Model for Aerosols: Description of Computational Analogs, J. Atmos. Sci., 45, 2123–2144, https://doi.org/10.1175/1520-0469(1988)045<2123:AMMFAD>2.0.CO;2, 1988.

Wang, H., Easter, R. C., Zhang, R., Ma, P., Singh, B., Zhang, K., Ganguly, D., Rasch, P. J., Burrows, S. M., Ghan, S. J., Lou, S., Qian, Y., Yang, Y., Feng, Y., Flanner, M., Leung, L. R., Liu, X., Shrivastava, M., Sun, J., Tang, Q., Xie, S., and Yoon, J.: Aerosols in the E3SM Version 1: New Developments and Their Impacts on Radiative Forcing, J. Adv. Model. Earth Syst., 12, https://doi.org/10.1029/2019MS001851, 2020.

Wang, Y., Liu, X., Hoose, C., and Wang, B.: Different contact angle distributions for heterogeneous ice nucleation in the Community Atmospheric Model version 5, Atmospheric Chemistry and Physics, 14, 10411–10430, https://doi.org/10.5194/acp-14-10411-2014, 2014.

Wylie, D. P., Menzel, W. P., Woolf, H. M., and Strabala, K. I.: Four Years of Global Cirrus Cloud Statistics Using HIRS, J. Climate, 7, 1972–1986, https://doi.org/10.1175/1520-0442(1994)007<1972:FYOGCC>2.0.CO;2, 1994.

Xuepeng, Z. and NOAA CDR Program: NOAA Climate Data Record (CDR) of AVHRR Daily and Monthly Aerosol Optical Thickness (AOT) over Global Oceans, Version 4.0. [1990-1993, monthly average], https://doi.org/10.25921/w3zj-4y48, n.d.

Zanchettin, D., Timmreck, C., Khodri, M., Schmidt, A., Toohey, M., Abe, M., Bekki, S., Cole, J., Fang, S.-W., Feng, W., Hegerl, G., Johnson, B., Lebas, N., LeGrande, A. N., Mann, G. W., Marshall, L., Rieger, L., Robock, A., Rubinetti, S., Tsigaridis, K., and Weierbach, H.: Effects of forcing differences and initial conditions on inter-model agreement in the VolMIP volc-pinatubo-full experiment, Geosci. Model Dev., 15, 2265–2292, https://doi.org/10.5194/gmd-15-2265-2022, 2022.

Zhao, T. X.-P., Stowe, L. L., Smirnov, A., Crosby, D., Sapper, J., and McClain, C. R.: Development of a Global Validation Package for Satellite Oceanic Aerosol Optical Thickness Retrieval Based on AERONET Observations and Its Application to NOAA/NESDIS Operational Aerosol Retrievals, J. Atmos. Sci., 59, 294–312, https://doi.org/10.1175/1520-0469(2002)059<0294:DOAGVP>2.0.CO;2, 2002.

Zhao, T. X.-P., Chan, P. K., and Heidinger, A. K.: A global survey of the effect of cloud contamination on the aerosol optical thickness and its long-term trend derived from operational AVHRR satellite observations, J. Geophys. Res. Atmos., 118, 2849–2857, https://doi.org/10.1002/jgrd.50278, 2013.

Zhao, Xuepeng: Climate Data Record (CDR) Program, Climate Algorithm Theoretical Basis Document (C-ATBD), AVHRR Aerosol Optical Thickness (AOT), 2022.